

## Berry Phase Effects of Nuclei in Chemical Reaction Dynamics

Xingyu Zhang, Jinke Yu, and Qingyong Meng<sup>a)</sup>

*Department of Chemistry, Northwestern Polytechnical University, West Youyi Road 127,  
710072 Xi'an, China*

(Dated: 9 July 2025)

**Abstract:** In calculations on quantum state-resolved dynamics of a chemical reaction, reactants are usually prepared in separated eigenstates of individual fragments, and their direct-product is then evolved in time. In this work, we focus on the essence in separating them and the Berry phase effects of the nuclear wave function. By the present theory, mechanism of inter/intramolecular energy redistribution is also proposed to deeply understand reactive dynamics with multivibrational states. To demonstrate the phase transition of the nuclear wave function, two three-dimensional (3D) models reductively describing the molecular reaction are developed to simulate transport of the system along a closed path in a parameter space represented of inter/intramolecular energy transfers. Employing these 3D models, extensive multiconfigurational time-dependent Hartree (MCTDH) calculations are performed to solve the time-dependent nuclear Schrödinger equation at various initial conditions. Moreover, 98D multilayer MCTDH (ML-MCTDH) calculations are launched to demonstrate the transition of Berry phase. These calculations clearly indicate that the wave function can change sign allowing quantum interference in the parameter space. Discussions on the separation of the reactants are made, while perspectives on the Berry phase effects predicted by the present work are given from the viewpoint of differential geometry. As a conclusion remark, the Berry phase effects on molecular dynamics are also thoroughly compared with those on electronic properties (see, for example, *Rev. Mod. Phys.* **82** (2010), 1959) and mode/bond-specific reactivity (see, for example, *Nat. Chem.* **14** (2022), 545).

**Keywords:** *Berry Phase; Molecular wave function; Chemical Reaction Dynamics; Adiabatic and Diabatic; Energy Redistribution*

---

<sup>a)</sup>Electronic mail: qingyong.meng@nwpu.edu.cn

## I. INTRODUCTION

Owing to the significant mass difference between electron and nuclear, chemical dynamics typically begins by approximately separating electronic and nuclear motions, called the Born-Oppenheimer approximation (BOA)<sup>1-3</sup>. It is the BOA which is not only gives rise to adiabatic and diabatic representations of a molecular system but also induces an additional phase in the electronic wave function<sup>4</sup>, called Berry phase. The concept of Berry phase is of immense interest across various fields of physics due to its (1) gauge invariance, (2) geometrical essence, and (3) analogies to gauge field theories and differential geometry. The Berry phase effects<sup>5</sup> lead subsequently to observable quantum interference in chemical reaction. This is one of quantum effects that are ubiquitous and crucial in understanding chemical reaction dynamics<sup>6-14</sup>. On the other hand, appropriate separation of degrees of freedom (DOFs) and the subsequent dimensionality reduction play an important role in quantum dynamics to significantly reduce computational costs. To do this, the DOFs of a high-dimensional system are firstly divided into distinct parts, such as fast or slow one, based on drastically different motion rates or frequencies, and then either the slow or fast DOFs are fixed at their optimal values according to chemical inspiration. For instance, in quantum dynamics calculations on  $\text{H} + \text{CH}_4 \rightarrow \text{H}_2 + \text{CH}_3$ , the  $\text{CH}_3$  fragment is usually fixed at the  $C_{3v}$  symmetry. In other words, the fast DOFs of  $\text{CH}_3$ , such as asymmetric C-H stretching modes, are separated and frozen. Alternatively, in dynamics calculations on surface scattering, the surface DOFs, *i.e.* the slow DOFs, are often frozen. Such scheme of separation and reduction is also employed in electronic structure where the nuclear coordinates are separated due to the BOA.

In this work, we focus on the Berry phase of nuclear wave function rather than that of electronic wave function. Over the past years, separation of the molecule and the surface during the surface scattering has been explored theoretically<sup>15,16</sup>, implicitly producing the Berry phase of molecular wave function, where the molecule and surface atoms are fast and slowly moving, respectively. In this analysis, the adiabatic and diabatic representations of the molecule-surface scattering were introduced. Here, we should mention that the adiabatic representation of a process assumes that a system undergoes a change without changing its surroundings, while the diabatic representation is the opposite of the adiabatic one allowing the system to exchange energy with its surroundings. Moreover, by the present theory, a new mechanism is proposed in this work for inter/intramolecular modes redistribution (IMR) which in a unique molecule also denotes intramolecular vibrational energy redistribution (IVR). The IMR process plays an important role in

chemical dynamics, especially noting that vibrational excitations often efficiently control chemical reactions<sup>17,18</sup>. A intuitive way based on dynamics calculations could provide a definitive measure of this process by the time evolutions of a limited number of accessible states. However, this way is often too simplistic to fully understand IMR at full quantum-mechanical fashion taking into account all the couplings. For instance, Pan and Liu<sup>11</sup> suggested that the scattering interferences mediated by the CH<sub>3</sub>D vibrational Fermi phases must be considered in understanding its reaction with Cl. By the present theory, one can construct a basis set of all possible rovibrational states (rather than electronic states) to establish a non-adiabatic representation. The dynamics calculations under this non-adiabatic representation will explicitly reveal the IMR processes among different rovibrational states during reaction.

The rest of this paper is organized as follows. Section II gives the present theory. Section III presents numerical demonstrations, together with discussions and perspectives. Section IV concludes with a summary.

## II. THEORY

### A. Adiabatic and Diabatic Representations

First of all, unless specified otherwise, the atomic units are always employed in this work. In a formalist way, a two-body system can be described by the point in the space  $\mathbf{z} = \{\mathbf{q}, \mathbf{Q}, \boldsymbol{\lambda}\}$ , which is direct sum of a parameter space  $\boldsymbol{\lambda}$  and the configurational space  $\{\mathbf{q}, \mathbf{Q}\}$ , where  $\mathbf{q}$  and  $\mathbf{Q}$  are coordinates of the two bodies. We further assume that  $\boldsymbol{\mathfrak{z}} = \mathbf{z} \setminus \mathbf{q}$ . Letting the Hamiltonian  $\hat{H}(\mathbf{z})$  be explicitly time-independent, in adiabatic evolution, where one of elements in  $\mathbf{z}$  varies very slowly, solution of the Schrödinger equation  $i\partial_t\Psi_n = \hat{H}\Psi_n$  is written as

$$\Psi_n(\mathbf{z}, t) = \exp(i\gamma_n(t)) \exp\left[-i \int_0^t dt' \epsilon_n(\mathbf{z}(t'))\right] \psi_n(\mathbf{z}(0)), \quad (1)$$

where  $n$  represents quantum numbers labeled the state. The function  $\psi_n(\mathbf{z}(0))$  is eigenstate of the Hamiltonian operator at initial time  $t = 0$ , while  $\epsilon_n(\mathbf{z}(t))$  is the eigenvalue corresponding to  $\psi_n(\mathbf{z}(t))$ , satisfying  $\hat{H}\psi_n = \epsilon_n\psi_n$ . The second exponential is known as the dynamical phase factor, while  $\gamma_n(t)$  is an additional phase. To understand  $\gamma_n$ , substituting Equation (1) into the Schrödinger equation, the phase  $\gamma_n$  is a path integral

$$\gamma_n = i \int_{\Gamma} d\boldsymbol{\mathfrak{z}} \langle \psi_n | \partial_{\boldsymbol{\mathfrak{z}}} | \psi_n \rangle_{\mathbf{q}} = \int_{\Gamma} d\boldsymbol{\mathfrak{z}} A_n(\boldsymbol{\mathfrak{z}}), \quad (2)$$

where  $\Gamma$  is integral path and  $A_n(\mathbf{z}) = i\langle\psi_n|\partial_{\mathbf{z}}|\psi_n\rangle_{\mathbf{q}}$  is the Berry connection. For a general path, one can always choose an appropriate gauge transform  $\psi_n \rightarrow \psi_n \exp(if)$  to cancel out  $\gamma_n$ . For a closed path, because  $\exp(if)$  must be single valued, one may not remove the phase

$$\gamma_n = \oint_{\Gamma} d\mathbf{z} A_n(\mathbf{z}). \quad (3)$$

In this case,  $\gamma_n$  becomes gauge-invariant, known as the Berry phase or geometric phase. If the above two-body system is a molecular system, letting the nuclear coordinates be slow DOFs, the above derivations and definitions on the Berry phase and the Berry connection lead to the Berry phase effects on electronic properties<sup>1-3</sup>. Furthermore, such derivations have been used to demonstrate the existence of a phase in the molecular wave function<sup>16</sup> by optimizing factorized wave function of the molecule-surface system<sup>2,3,16</sup>.

To separate the DOFs of the above two-body system, let us derive equations of motion (EOMs) for these bodies. Assuming that the sets of mass-scaled coordinates  $\mathbf{q}$  and  $\mathbf{Q}$  describe the fast and slow motions of a reaction system, respectively. The Hamiltonian operator can be written as summation of the kinetic energy operator (KEO) for the slow DOFs and the Hamiltonian operator for the fast DOFs,

$$\hat{H}(\mathbf{z}) = \hat{T}_{\text{slow}}(\mathbf{Q}, \boldsymbol{\lambda}) + \hat{H}'_{\text{fast}}(\mathbf{z}) = \hat{T}_{\text{slow}}(\mathbf{Q}, \boldsymbol{\lambda}) + \hat{T}_{\text{fast}}(\mathbf{q}, \boldsymbol{\lambda}) + V_{\text{fast}}(\mathbf{q}, \mathbf{Q}_0, \boldsymbol{\lambda}) + V_{\text{slow}}(\mathbf{Q}, \boldsymbol{\lambda}) + V_{\text{coul}}(\mathbf{z}), \quad (4)$$

where  $V_{\text{fast}}$  is the potential energy surface (PES) for the fast motions with the slow coordinates fixed at  $\mathbf{Q}_0$ , while  $V_{\text{slow}}$  is the PES for the slow motions. Moreover,  $V_{\text{coul}}$  is the coupling term between the fast and slow DOFs. Inspiring by factorization for the molecule-surface system<sup>16</sup>, the wave function of the entire system  $\Psi(\mathbf{z})$  is factorized into a term  $\varphi(\mathbf{z})$  for the fast motions and a term  $\chi(\mathbf{z})$  for the slow motions,

$$\Psi(\mathbf{z}) = \varphi(\mathbf{z})\chi(\mathbf{Q}, \boldsymbol{\lambda}) = \varphi(\mathbf{z})\chi(\mathbf{z}), \quad (5)$$

where  $\varphi$  depends parametrically on  $\mathbf{Q}$  and is normalized  $\langle\varphi|\varphi\rangle_{\mathbf{q}} = 1$ , while we again assume that  $\mathbf{z} = \mathbf{z} \setminus \mathbf{q}$ . Now, we should optimize  $\varphi$  and  $\chi$  with normalization conditions  $\langle\varphi|\varphi\rangle_{\mathbf{q}} = 1$  and  $\langle\Psi|\Psi\rangle_{\mathbf{q}} = 1$  to improve the form of the Hamiltonian operator of Equation (4) and to derive the EOMs for  $\varphi$  and  $\chi$  such that  $\Psi$  is automatically factorized as given in Equation (5). Letting  $\mu_1$  and  $\mu_2$  be Lagrange parameters, the optimization target reads

$$\mathcal{J}[\varphi, \chi] = \langle\varphi\chi|\hat{H}|\varphi\chi\rangle_{\mathbf{q}} + \mu_1(1 - \langle\varphi\chi|\varphi\chi\rangle_{\mathbf{q}}) + \mu_2(1 - \langle\chi|\chi\rangle_{\mathbf{Q}}). \quad (6)$$

Varying  $\mathcal{J}$  with respect to  $\varphi$  and  $\chi$  and setting to zero, namely  $\delta\mathcal{J}/\delta\varphi = 0$  and  $\delta\mathcal{J}/\delta\chi = 0$ , one can obtain

$$\hat{H}_{\text{fast}}\varphi - \langle\varphi|\hat{H}_{\text{fast}}|\varphi\rangle_q\varphi = (\hat{H}_{\text{fast}} - E)\varphi = 0, \quad (\hat{T}_{\text{slow}} + E)\chi = \mu_1\chi, \quad (7)$$

where  $E = \langle\varphi|\hat{H}_{\text{fast}}|\varphi\rangle_q$  is expectation of the effective Hamiltonian operator for the fast motions,

$$\hat{H}_{\text{fast}} = \hat{T}_{\text{slow}} + \hat{H}'_{\text{fast}} - (\nabla_{\mathbf{Q}} \ln \chi) \nabla_{\mathbf{Q}} = \hat{H} - (\nabla_{\mathbf{Q}} \ln \chi) \nabla_{\mathbf{Q}}. \quad (8)$$

In deriving Equations (7) and (8), one can further find  $\mu_2 = 0$ . Thus, the separation of fast and slow DOFs of the system is mathematically similar to that of the electrons and nuclei in the molecular system. According to Equation (8), the effective Hamiltonian operator  $\hat{H}_{\text{fast}}$  has an additional term  $-(\nabla_{\mathbf{Q}} \ln \chi) \nabla_{\mathbf{Q}}$  that arises a phase in  $\varphi$ . To observe the phase term, we must further consider the *adiabatic* and *diabatic* representations of the entire system involved in multiple rovibrational states.

To this end, assuming  $\varphi_j$  the  $j$ -th eigenstate of  $\hat{H}'_{\text{fast}}$ , one can extend Equation (5) into the  $N$ -states expansion,

$$\Psi(\mathbf{z}) = \sum_j^N \varphi_j(\mathbf{z}) \chi_j(\mathfrak{z}), \quad (9)$$

where the  $j$ -th coefficient  $\chi_j$  is the  $j$ -th element of the representation of  $\Psi$ , that is matrix  $\Psi(\mathbf{z})$ . Substituting Equation (9) into the Schrödinger equation with  $\hat{H}$ , one can obtain

$$-\frac{1}{2}\nabla_{\mathfrak{z}}^2\Psi + (\mathbf{E} - \mu_1\mathbf{I})\Psi - \frac{1}{2}(2\boldsymbol{\tau} \cdot \nabla_{\mathbf{q}} + \boldsymbol{\tau}^{(2)})\Psi = \mathbf{0}, \quad (10)$$

where  $\mathbf{E}$  and  $\mu_1$  are matrix with elements  $E_{ij} = \langle\varphi_i|\hat{H}'_{\text{fast}}|\varphi_j\rangle_q = E_i\delta_{ij}$  and eigenvalue of  $\hat{H}_{\text{slow}}$ , respectively, as shown by Equation (7). Moreover, the elements of non-adiabatic coupling matrix (NACM)  $\boldsymbol{\tau}$  and second-order NACM  $\boldsymbol{\tau}^{(2)}$  satisfy expressions  $\tau_{ij} = \langle\varphi_i|\nabla_{\mathfrak{z}}|\varphi_j\rangle_q$  and  $\tau_{ij}^{(2)} = \langle\varphi_i|\nabla_{\mathfrak{z}}^2|\varphi_j\rangle_q$ , respectively. Noting that  $\nabla_{\mathbf{q}} \cdot \boldsymbol{\tau} = \boldsymbol{\tau}^{(2)} - \boldsymbol{\tau}^2$ , one can eliminate  $\boldsymbol{\tau}^{(2)}$  from Equation (10) and obtain adiabatic EOM

$$-\frac{1}{2}(\nabla_{\mathfrak{z}} + \boldsymbol{\tau})^2\Psi + (\mathbf{E} - \mu_1\mathbf{I})\Psi = \mathbf{0}. \quad (11)$$

Turning to the diabatic representation, the wave function is expanded by

$$\tilde{\Psi}(\mathbf{z}) = \sum_j^N \varphi_j(\mathbf{z}_0) \tilde{\chi}_j(\mathfrak{z}), \quad (12)$$

where  $\mathbf{z}_0 = \{\mathbf{q}, \mathbf{Q}_0, \boldsymbol{\lambda}\}$  is obtained from  $\mathbf{z}$  by fixing  $\mathbf{Q}$  at  $\mathbf{Q}_0$ . Similar to  $\{\varphi_j(\mathbf{z})\}_{j=1}^N$  in expansion of Equation (9), the set  $\{\varphi_j(\mathbf{z}_0)\}_{j=1}^N$  is an approximately complete set of eigenstates for  $\hat{H}'_{\text{fast}}(\mathbf{z}_0)$ .

Substituting Equation (12) into the Schrödinger equation with  $\hat{H}$ , one can obtain diabatic EOM

$$-\frac{1}{2}\nabla_{\mathfrak{z}}^2\tilde{\Psi} + (\mathbf{V} - \mu_1\mathbf{I})\tilde{\Psi} = \mathbf{0}. \quad (13)$$

where the diabatic potential matrix  $\mathbf{V}(\mathfrak{z})$  has the element  $V_{ij}(\mathfrak{z}) = \langle \varphi_i(\mathbf{z}_0) | \hat{H}'_{\text{fast}}(\mathbf{z}) | \varphi_j(\mathbf{z}_0) \rangle_q$ . Due to the difference between  $\mathbf{z}_0$  and  $\mathbf{z}$ , the matrix  $\mathbf{V}$  is non-diagonal.

## B. The Phase Effects of Nuclear Wavefunction

The transform between the adiabatic and diabatic representations requires transform matrix between  $\varphi(\mathbf{z})$  and  $\varphi(\mathbf{z}_0)$ . Solving first-order expansional expression  $\nabla_q \varphi(\mathbf{z}) + \boldsymbol{\tau} \cdot \varphi(\mathbf{z}) = \mathbf{0}$  from  $\mathbf{z}_1$  to  $\mathbf{z}_2$ , one can obtain  $\varphi(\mathbf{z}_2) = \varphi(\mathbf{z}_1) - \int_{\mathbf{z}_1}^{\mathbf{z}_2} d\mathbf{z}' \cdot \boldsymbol{\tau}(\mathbf{z}') \cdot \varphi(\mathbf{z}')$ . If  $\mathbf{z}_1 = \mathbf{z}_2$ , the above integral along a closed path  $\Gamma$  in the space  $\mathbf{z}$  is given by

$$\varphi(\mathbf{z}; \Gamma) = \varphi(\mathbf{z}) - \oint_{\Gamma} d\mathbf{z}' \cdot \boldsymbol{\tau}(\mathbf{z}') \cdot \varphi(\mathbf{z}'). \quad (14)$$

Comparing with Equation (3), the second term in the right-hand side of Equation (14) can be recognized as the Berry phase while the NACM  $i\boldsymbol{\tau}(\mathbf{z})$  can be recognized as the Berry connection. To further explore this point, Equation (14) is rewritten as

$$\varphi(\mathbf{z}; \Gamma) = \mathcal{P} \exp\left(-\oint_{\Gamma} d\mathbf{z}' \cdot \boldsymbol{\tau}(\mathbf{z}')\right) \varphi(\mathbf{z}), \quad (15)$$

where  $\mathcal{P}$  represents sequential integration carried out over the space  $\mathbf{z}$ . Comparing Equation (3) with Equation (15), one can find

$$\varphi_j(\mathbf{z}_0; \Gamma) = \exp(i\gamma_j(\Gamma))\varphi_j(\mathbf{z}_0), \quad j = 1, 2, \dots, N. \quad (16)$$

Similar to the separation between electron and nuclear in the molecule, if the parameter space  $\mathbf{z}$  changes along the closed loop  $\Gamma$ , the wave function for the fast motions undergoes a phase change. For clarity, we compare the present phase effects with those on electronic structure in Table I. The agreement between both separation theories is evident that they both focus on the dynamics of fast motions.

Equations (11) and (13) give the time-independent EOMs of the adiabatic and diabatic representations, respectively. If both  $\Psi$  and  $\tilde{\Psi}$  are explicitly time-dependent, one can similarly and directly extend the time-independent EOMs to,

$$i\frac{\partial}{\partial t}\Psi(t) = \left[-\frac{1}{2}(\nabla_{\mathfrak{z}} + \boldsymbol{\tau})^2 + \mathbf{E}\right]\Psi(t) = \mathbf{H}_{\text{adia}}\Psi(t), \quad i\frac{\partial}{\partial t}\tilde{\Psi}(t) = \left(-\frac{1}{2}\nabla_{\mathfrak{z}}^2 + \mathbf{V}\right)\tilde{\Psi}(t) = \mathbf{H}_{\text{dia}}\tilde{\Psi}(t), \quad (17)$$

where  $\mathbf{H}_{\text{adia}}$  and  $\mathbf{H}_{\text{dia}}$  are time-independent Hamiltonian matrices of the adiabatic and diabatic representations, respectively. By solving Equation (17), one can elucidate the mechanism of IMR, say the IVR process, which is analogous to understand how a molecule evolves among various electronic states. We must mention that the relation between  $\mathbf{E}$  and  $\mathbf{V}$  is usually unknown. To overcome this problem, we approximately rewrite Equation (17) as

$$i\frac{\partial}{\partial t}\tilde{\Psi}(t) = \left(-\frac{1}{2}\nabla_{\mathbf{s}}^2 + \mathbf{U}\right)\tilde{\Psi}(t) = \mathbf{H}_{\text{nonadia}}\tilde{\Psi}(t). \quad (18)$$

where  $\mathbf{H}_{\text{nonadia}}$  and  $\mathbf{U}$  mean nonadiabatic Hamiltonian and potential matrices, respectively, of the fast motions. To construct  $\mathbf{U}$ , appropriate models must be developed to account for inter-state couplings during IMR. Similar to Equation (1), since  $\mathbf{H}_{\text{adia}}$  and  $\mathbf{H}_{\text{dia}}$  are both time-independent, propagating the  $j$ -th state of the system along the closed path  $\Gamma$  in the parameter space, one can obtain

$$\tilde{\Psi}_j(\mathbf{z}_0, t; \Gamma) = \tilde{\Psi}_j(\mathbf{z}_0, t) \exp(i\gamma_j(t; \Gamma)), \quad (19)$$

where the dynamical phase factor has been absorbed into the  $\tilde{\Psi}_j(\mathbf{z}_0, t)$  term. According to Equation (19), the autocorrelation function for the fast motions undergoes a phase.

Next, let us turn to the effect of the parameter set  $\lambda$  and introduce the concept of so-called pathological point in the configurational space. The core idea is that the inequality  $\oint_{\Gamma} d\mathbf{z}' \cdot \boldsymbol{\tau}(\mathbf{z}') \neq 0$  does not imply the existence of  $\oint_{\Gamma} d\mathbf{Q}' \cdot \boldsymbol{\tau}(\mathbf{z}') \neq 0$ . Thus, only integral along the closed path in the configurational space  $\mathbf{Q}$  may not indicate a nonzero phase. Moreover, it is possible to find a pathological point in the configurational space such that  $\oint_{\Gamma} d\mathbf{Q}' \cdot \boldsymbol{\tau}(\mathbf{z}') \neq 0$  when  $\Gamma$  encircles that pathological point. As given by Table I, the pathological point in the electronic-structure theory is conical intersection (CI) between adjacent electronic states. To topologically illustrate the CI point, the PESs should be expressed as a function of the branch space  $g$ - $h$  near CI, where the gradient difference  $g$  describes the gradient difference between the two electronic states, while the non-adiabatic coupling  $h$  describes the strength of coupling. Both  $g$  and  $h$  can be seen as parameters of electronic structure. For the present theory on separation of the fast and slow DOFs in the reaction, a similar pathological point in the configurational space might not exist. However, it is still possible to find  $\oint_{\Gamma} d\mathbf{z}' \cdot \boldsymbol{\tau}(\mathbf{z}') \neq 0$  where  $\Gamma$  can be found in the parameter space  $\lambda$  that represents environmental conditions of the reaction. For instance, we previously proposed two-dimensional coupled harmonic oscillators (2D CHO) model<sup>15,19</sup> to explain the coupling in the molecule-surface scattering, where the masses and frequencies are  $\{m, M\}$  and  $\{\omega, \Omega\}$ , respectively, while the ratio  $\Omega/\omega$  represents the surface temperature. As previously discussed<sup>15,19</sup>, the 2D CHO model predicts

that at  $\Omega/\omega = \sqrt{1 - m/M}$  an assignment between two oscillators becomes unclear, rather than individual motion, called critical point. This is similar to the situation where the reaction occurs very fastly through the CI point and thus motions of the electrons and nuclei can not be separately considered at CI. It is also clear that the IER (or IVR) process requires the aid of the slow motions. It should be mentioned that the IER process is arisen from the couplings between the modes associated with the slow motions, such as the surface motions in surface scattering. For example, as expected by quantum dynamics calculations, the surface phonons play an central role in the IVR process of the molecule-surface scattering.

### III. RESULTS AND DISCUSSIONS

#### A. Models for Chemical Reaction

To demonstrate the present theory for chemical reactions, we firstly introduce two numerical models for the simplest three-body reactions and surface scattering. By these models, numerical demonstrations on the present theory will be given and discussed. The first one is model for surface scattering of a diatomic molecule. As previously discussed<sup>15,16</sup> on the 2D CHO model for the absorbed molecule on the surface, the avoided crossing scenario of the vibrational eigenenergies in frequencies space was demonstrated, where the surface atom is bound harmonically to its equilibrium position and the molecule is bound harmonically to the surface atom. However, the 2D CHO model<sup>15,16</sup> cannot simulate internal motions of the adsorbed molecule. To overcome this problem, the 2D CHO model<sup>15,16</sup> is extended to a three-dimensional (3D) CHO model, as illustrated in Figure 1, where  $\{m_i\}_{i=1}^3$  and  $\{q_i\}_{i=1}^3$  represent mass and coordinate sets of the oscillators, respectively, while  $\{\omega_i\}_{i=1}^3$  denotes associated frequencies set. Figure 1 implies that  $\omega_1$  and  $\omega_3$  model the intramolecular potentials, while  $\omega_2$  models the molecule-surface potential. According to Figure 1, the 3D CHO Hamiltonian reads

$$\begin{aligned}
2\hat{H}_{\text{3D-CHO}}(q_1, q_2, q_3, \eta, \xi) &= \frac{\hat{p}_1^2}{m_1} + \frac{\hat{p}_2^2}{m_2} + \frac{\hat{p}_3^2}{m_3} + m_3\omega_3^2q_3^2 + m_1\omega_1^2(q_1 - q_2)^2 + m_2\omega_2^2(q_2 - q_3)^2 \\
&= \hat{p}_1^2 + \hat{p}_2^2 + \hat{p}_3^2 + \omega_3^2\tilde{q}_3^2 + \omega_1^2(\tilde{q}_1 - \zeta_1\tilde{q}_2)^2 + \omega_2^2(\tilde{q}_2 - \zeta_2\tilde{q}_3)^2 \\
&= \hat{p}_1^2 + \hat{p}_2^2 + \hat{p}_3^2 + \omega_2^2 \begin{pmatrix} \tilde{q}_1 & \tilde{q}_2 & \tilde{q}_3 \end{pmatrix} \begin{pmatrix} \eta & -\zeta_1\eta & 0 \\ -\zeta_1\eta & 1 + \zeta_1^2\eta & -\zeta_2 \\ 0 & -\zeta_2 & \xi + \zeta_2^2 \end{pmatrix} \begin{pmatrix} \tilde{q}_1 \\ \tilde{q}_2 \\ \tilde{q}_3 \end{pmatrix}, \quad (20)
\end{aligned}$$

where  $\tilde{q}_i = \sqrt{m_i}q_i$  and  $\tilde{p}_i = p_i/\sqrt{m_i}$  with  $i = 1, 2, 3$ , are mass-scaled coordinates and momenta, respectively. We also define the frequency parameters as  $\eta = \omega_1^2/\omega_2^2$  and  $\xi = \omega_3^2/\omega_2^2$  and coupling paramters as  $\zeta_1 = \sqrt{m_1/m_2}$  and  $\zeta_2 = \sqrt{m_2/m_3}$ . The set of  $\{\xi, \eta\}$  is thus the parameter space of the 3D CHO model. The frequencies of the normal mode are related to the eigenvalues of the  $3 \times 3$  potential matrix in Equation (20). Unlike the 2D CHO model that exhibits an avoided crossing region<sup>15,16</sup>, eigenvalues of the 3D CHO model as functions of  $\eta$  and  $\xi$  have degeneracy seams, whose projection on  $\eta$  is critical point  $\eta_c$ . Analyzing degeneracy of the eigenvalues, the critical point  $\eta_c$  only depends on the mass of the fragments, namely  $\eta_c = \sqrt{1 + m_1/\max(m_2, m_3)}$ . This implies that the degeneracy feature is an intrinsic properties of the system. Such discrepancy between avoided crossing and degeneracy seam is arisen from that two restrictions on the system must be simultaneously satisfied for existence of degenerated states. Since eigenstate of the 2D CHO model<sup>15,16</sup> has only one variable, that is frequency ratio of two oscillators, its eigenstates cannot be degenerate. The situation of the 3D CHO model changes due to its two variables,  $\eta$  and  $\xi$ , where its eigenstates are possibly degenerated at one-dimensional (1D) seam lines or zero-dimensional seam points. We would like to finally emphasize that Equation (20) holds by expanding the three-body interactions to second-order Taylor expansions with omission of anharmonic contributions and assumptions of negligible interaction between  $m_1$  and  $m_3$ .

Next, we turn to model for a bimolecular reaction (REX) which can be reduced to a simple three-fragment exchange process described by the Jacobi coordinates set  $\{r_v, r_d, \theta\}$ , called 3D REX model. Three fragments labeled by #1, #2, and #3 have masses  $\{m_i\}_{i=1}^3$ , where the fragment #1 is the colliding group and the fragments #2 and #3 the target. As the reaction coordinates, vector  $\vec{r}_v$  is from  $m_2$  to  $m_3$ ,  $\vec{r}_d$  from  $m_1$  to the center-of-mass (COM) of the other two fragments, while  $\theta$  is the angle between  $\vec{r}_v$  and  $\vec{r}_d$ . For simple, the total rotations of the entire system is ignored by setting the total angular momentum to be zero. With the above assumptions, the PES of the 3D REX model reads  $V_{3D-REX} = V_3 + V_{rev}$ . The  $V_3$  term is a 3D model potential along the reaction coordinates based on the BKMP2 PES of the H + H<sub>2</sub> system<sup>20</sup> and produces main features for the bimolecular reaction. The  $V_{rev}$  term is the revision and perturbation due to the coupling between the reaction coordinate and the others. Similar to the derivation of Equation (20), assuming that interactions between each pairs of fragments are truncated at the second order, we have

$$2V_{rev}(r_v, r_d, \theta, \alpha, \beta) = \omega_{23}^2 \left[ (\mu_{23} + \kappa_1\alpha + \kappa_2\beta)r_v^2 + (\mu_{12}\alpha + \mu_{13}\beta)r_d^2 - \frac{1}{v_{23}}(\kappa_1m_2\alpha - \kappa_2m_3\beta)r_v r_d \cos \theta \right], \quad (21)$$

where

$$\mu_{12} = \frac{m_1 m_2}{m_1 + m_2}, \quad \mu_{13} = \frac{m_1 m_3}{m_1 + m_3}, \quad \mu_{23} = \frac{m_2 m_3}{m_2 + m_3}, \quad \kappa_1 = \mu_{12} \left( \frac{\mu_{23}}{m_2} \right)^2, \quad \kappa_2 = \mu_{13} \left( \frac{\mu_{23}}{m_3} \right)^2. \quad (22)$$

Letting  $\{\omega_{ij}\}_{i,j=1}^3$  be frequencies between two distinct fragments, the parameters  $\alpha$  and  $\beta$  in Equation (21) satisfy

$$\alpha = \frac{\omega_{12}^2}{\omega_{23}^2}, \quad \beta = \frac{\omega_{13}^2}{\omega_{23}^2}. \quad (23)$$

Therefore, the Hamiltonian of the present 3D REX model is given by

$$2\hat{H}_{3\text{D-REX}}(r_v, r_d, \theta, \alpha, \beta) = -\frac{1}{\mu} \frac{\partial^2}{\partial r_d^2} - \frac{1}{\mu_{23}} \frac{\partial^2}{\partial r_v^2} - \left( \frac{1}{\mu r_d^2} + \frac{1}{\mu_{23} r_v^2} \right) \frac{1}{\sin \theta} \frac{\partial}{\partial \theta} \sin \theta \frac{\partial}{\partial \theta} + 2V_{3\text{D-REX}}(r_v, r_d, \theta, \alpha, \beta), \quad (24)$$

where  $\mu = m_1(m_2 + m_3)/(m_1 + m_2 + m_3)$  is the reduced mass associated with  $r_d$ . As illustrated by the surface plots and contour plots of  $V_{3\text{D-REX}}$  in Figure 2, the term  $V_{\text{rev}}$  in Equation (21) is set to be a perturbation of  $V_3$  and thus  $V_{3\text{D-REX}} = V_3 + V_{\text{rev}}$  is approximately a mass model of chemical reaction.

Collected in Tables II and III are parameters of the present model Hamiltonian operators. Given in Table IV are primitive basis functions of discrete variable representation (DVR)<sup>21,22</sup>, together with the number of the grid points and the range of the grids which are all used for representing the present calculations through the multiconfigurational time-dependent Hartree (MCTDH) method<sup>23-27</sup>. According to Equations (20) and (24), almost all of KEO and PES terms are already given in a sum-of-products (SOP) form except for the  $V_3$  term. Since the MCTDH calculations need the Hamiltonian operator in the SOP form, the potential re-fitting (POTFIT) calculations<sup>28,29</sup> have to be firstly performed to transfer the  $V_3$  term into the SOP form. We refer the reader to Reference<sup>30</sup> for numerical details of the POTFIT calculations on the H + H<sub>2</sub> system. The re-fitting error of present POTFIT calculation is smaller than 1 meV ensuring accuracy of subsequent MCTDH calculations. We refer the reader to References<sup>31-36</sup> for further details on the MCTDH and POTFIT methods. By propagated wave function  $\Psi(t)$ , one can compute time-dependent phase angle for various models, as illustrated by Figure 3. According to Equation (1), the phase of  $\Psi(t)$  should be linear function of time if energy is conserved and there is no transition of the phase angle. Therefore, a slight deviation from the linear relationship in Figure 3, in particular that in Figure 3(b) for 3D REX model, implies changes in energy during the reaction process as well as phase changes during the parameter variation. We shall return to this point later after show the transition of phase angle at the critical point.

## B. Numerical Demonstrations

Figure 4 illustrates time-dependent phase angle of the nuclear wave functions computed by MCTDH with the 3D CHO model. The initial conditions and parameters are set to simulate different systems, as given by Tables II and III, including CO/Cu, CH<sub>4</sub>/Au, H<sub>2</sub>O, and H + H<sub>2</sub>. In Figure 4, the horizontal axis gives propagation time, while the left and right vertical axes indicate the phase angle and the time-dependent expectation of parameter  $\eta$ ,

$$\langle \eta \rangle(t) = \frac{\langle \Psi(t) | \eta | \Psi(t) \rangle}{\langle \Psi(t) | \Psi(t) \rangle}, \quad (25)$$

respectively. For the 3D CHO model, the inner product  $\langle \Psi(t) | \Psi(t) \rangle$  remains time-independent because the Hamiltonian  $\hat{H}_{3D-CHO}$  has no absorbing potential. In Figure 4, the blue symbol  $\times$  means the critical point  $\eta_c = \sqrt{1 + m_1 / \max(m_2, m_3)}$  (referred to the right axis), where the phase should change. As shown in Figure 4(a) for CO/Cu, the phase angle changes at  $t \sim 178$  fs, while the computed expectation  $\langle \eta \rangle$  of 1.204 is very close to the critical point of 1.119. Similarly, as shown in Figure 4(b) for CH<sub>4</sub>/Au, the phase angle changes at  $\sim 950$  fs where the computed  $\langle \eta \rangle$  value of 1.107 is close to the critical point of 1.037. The similar situation can be found in Figure 4(c) for H<sub>2</sub>O, where the phase angle changes at  $\sim 48$  fs and computed  $\langle \eta \rangle$  of 0.907 is close to the critical point of 1.031. Moreover, the order of critical times perfectly follows the sequence of mass magnitudes, CH<sub>4</sub>/Au (212.967 dalton and  $\sim 950$  fs), CO/Cu (91.546 dalton and  $\sim 178$  fs), and H<sub>2</sub>O (18.000 dalton and  $\sim 48$  fs). Turning to Figure 4(d) for H + H<sub>2</sub>, however, the situation changes slightly where the phase angle becomes linear dependence on time after  $\sim 10.2$  fs with computed  $\langle \eta \rangle$  value of 0.597 that is largely smaller than the critical point of  $\sqrt{2}$ . But, one can still find a change of phase angle from  $\sim \pi$  to zero at  $\sim 10.2$  fs, which indicates that the wave function changes its sign.

Having shown the results of bounded models through the 3D CHO Hamiltonian, we turn to Figure 5 for the time-dependent phase angle computed by the 3D REX model. Similar to Figure 4, the initial conditions and parameters are set to simulate different molecular systems, as given by Tables II and III. Results for these systems are illustrated by subfigures (a)-(d) for CO/Cu, CH<sub>4</sub>/Au, H<sub>2</sub>O, and H + H<sub>2</sub>, respectively. In Figure 5, the time-dependent expectations  $\langle \eta \rangle(t)$  are also illustrated by red lines where the inner product of  $\Psi(t)$  remains time-independent due to no absorbing potential in the Hamiltonian. Again, the blue symbol  $\times$  means the critical point  $\eta_c$ . Moreover, since the phase of H + H<sub>2</sub> changes dramatically, one cannot clearly find transition of the phase angle and thus the time where the critical point  $\sqrt{2}$  occurs. For clarity, the critical point

is given by a blue dashed line in Figure 5(d). As shown in Figure 5(a) for CO/Cu, the phase angle changes at  $t \sim 266$  fs, while the computed expectation  $\langle \eta \rangle$  of 1.504 is close to the critical point of 1.119. The similar situation can be found in Figure 5(c) for H<sub>2</sub>O, where the phase angle changes at  $\sim 34$  fs and computed  $\langle \eta \rangle$  of 1.667 is approximately close to the critical point of 1.031. As shown in Figure 5(b), the phase angle for CH<sub>4</sub>/Au has an almost constant plateau in the region of 238  $\sim$  242 fs. By Equation (1), although there is no phase transition, a discontinuous phase change exists if the dynamical phase is subtracted. Based on the phase reduction rate of  $\pi/2$  per fs as illustrated in Figure 5(b), the geometric phase angle would have undergone a shift of nearly  $\pi$  over the time interval 238  $\sim$  242 fs. At  $\sim 240$  fs the computed  $\langle \eta \rangle$  value of 1.728 is approximately close to the critical point of 1.037. Turning to Figure 5(d) for H + H<sub>2</sub>, the situation becomes unclear where the phase angle becomes linear dependence on time after  $\sim 35$  fs. Below 30 fs, the phase angle changes with amplitude of  $2\pi$  (at  $\sim 10$  fs) or  $4\pi$  (at  $\sim 20$  fs). At  $\sim 33$  fs, there is a phase angle change of  $\pi$  with computed  $\langle \eta \rangle$  value of 0.381 that is largely smaller than the critical point of  $\sqrt{2}$ . This indicates that the wave function changes its sign at  $\sim 33$  fs but changes phase angle below 30 fs. For clarity, the critical point is shown by a blue dashed line in Figure 5(d).

Comparing phase results for CH<sub>4</sub>/Au and CO/Cu (see Figures 4(a)-(b) and 5(a)-(b)) with those for H<sub>2</sub>O and H + H<sub>2</sub> (see Figures 4(c)-(d) and 5(c)-(d)), one can find the following two features. If  $m_3$  is very larger than  $m_1$  and  $m_2$ , as shown by results for CO/Cu and CH<sub>4</sub>/Au, the phase angle just changes by  $\pi$  near the critical point  $\eta_c$ , maintaining an approximately linear relationship with time throughout the other propagation duration (see the black and red lines of Figure 3). If  $m_3$  is not very large or even relatively small, as shown by results for H<sub>2</sub>O and H + H<sub>2</sub>, the phase angle remains nearly constant in the early propagation steps, changes by  $\pi$  and then exhibits an approximately linear relationship with time (see the blue and green lines of Figure 3). The linear relationship between the phase angle and time can be found by the dynamical phase in Equation (1). Moreover, for larger difference between  $m_3$  and  $\max m_1, m_2$ , the phase varies more smoothly over time than that for smaller difference, where the phase changes with more fluctuations as illustrated in Figure 3. Such significant differences in phenomena should be arisen from the mass difference between  $m_3$  and  $\max m_1, m_2$ . Comparing the 3D REX model with the 3D CHO model, one can find the following two different points. First, comparing resulting for CH<sub>4</sub>/Au (212.967 dalton and  $\sim 240$  fs) with those for CO/Cu (91.546 dalton and  $\sim 266$  fs), the order of critical times might not follow the sequence of mass magnitudes. It should be noted that difference of 26 fs between 240 fs and 266 fs is rather small and the reaction time based on the unperturbed

$V_3$  term is about 300 fs, which is very close to the critical times of 240 fs and 266 fs. Thus, the mass ordering inversion is not a major concern. Second, the 3D CHO model describes the linear relationship between the phase and time, together with the phase transition phenomena better than the 3D REX model. This might be arisen from the fact that the CHO and REX models focus on bound state and scattering state, respectively. Bound states typically conserve energy and exhibit linear relationship between phase and time, whereas scattering states may violate energy conservation (particularly when an complex absorbing potential is introduced), showing irregular phase changes.

Having demonstrated the present theory by the 3D CHO and 3D REX models, next we should turn to numerical demonstrations on high-dimensional model, where the atomic arrangement is given in Figure 6. Based on the present 3D CHO model (see Equation (20) and Figure 1), a model of a diatomic molecule adsorbed on a metal surface is proposed, where the masses and frequencies are set to be  $\{m_1, m_2, m_3\}$  and  $\{\omega_1, \omega_2, \omega_3\}$ , respectively. For simple, the CO/Cu(100) system is chosen as the benchmark. The Cu(100) surface is supposed to be a three-layer grid with 30 atoms with mass  $m_3 = 63.546$  dalton and coordinates  $\{Q_i\mu\}_{i=0}^{29}$ , where the atom #0 is the top site, the atoms #1-#8 the first layer, the atoms #9-#20 the second layer, the atoms #21-#29 the third layer (see Figure 6). The molecular motions are abstractly described by coordinates set  $\mathbf{q} = \{b, \chi, \phi\} \oplus \{R, \vartheta, z\}$ . The internal coordinates set  $\{b, \chi, \phi\}$  describes the C-O stretch and two-dimensional rotation of CO with polar angle  $\chi$  and azimuthal angle  $\phi$ , while  $\{R, \vartheta, z\}$  describes rotation of the entire molecule along a loop with radius  $R_0$  and angle  $\vartheta$ . By Equations (4), the Hamiltonian is given by

$$\hat{H} = \hat{H}_{\text{mol}} + \hat{H}'_{\text{surf}} + \hat{H}_{\text{3D-CHO}} = \hat{T}_{\text{mol}} + \hat{V}_{\text{mol}} + \hat{T}'_{\text{surf}} + \hat{V}'_{\text{surf}} + \hat{H}_{\text{3D-CHO}}. \quad (26)$$

where  $\hat{H}_{\text{mol}}$  and  $\hat{H}'_{\text{surf}}$  describe motions of CO and Cu(100), respectively, while  $\hat{H}_{\text{3D-CHO}}$  is the coupling term between CO and Cu(100) and given by Equation (20). The Hamiltonian  $\hat{H}_{\text{mol}}$  for CO reads

$$\begin{aligned} \hat{H}_{\text{mol}} &= \hat{T}_{\text{mol}} + \hat{V}_{\text{mol}} \\ &= -\frac{1}{2m} \left[ \frac{1}{b^2} \frac{\partial}{\partial b} \left( b^2 \frac{\partial}{\partial b} \right) + \frac{1}{b^2 \sin \chi} \frac{\partial}{\partial \chi} \left( \sin \chi \frac{\partial}{\partial \chi} \right) + \frac{1}{b^2 \sin^2 \chi} \frac{\partial^2}{\partial \phi^2} \right] \\ &\quad - \frac{1}{2(m_1 + m_2)} \left( \frac{1}{R} \frac{\partial}{\partial R} R \frac{\partial}{\partial R} + \frac{1}{R^2} \frac{\partial^2}{\partial \vartheta^2} \right) + \frac{1}{2} k_b (b - b_0)^2 + \frac{1}{2} k_R (R - R_0)^2, \end{aligned} \quad (27)$$

where  $m = m_1 m_2 / (m_1 + m_2)$  is the reduced mass of CO. The radial potential  $\hat{V}_{\text{mol}} = k_R (R - R_0)^2 / 2$  ensures that the CO molecule always move along the closed loop. Motions of the Cu(100) surface

are described by<sup>37</sup>

$$\hat{H}'_{\text{surf}} = -\frac{1}{2m_3} \sum_{\mu=x,y} \frac{\partial^2}{\partial Q_{0\mu}^2} - \frac{1}{2m_3} \sum_{i=1}^{29} \sum_{\mu=x,y,z} \frac{\partial^2}{\partial Q_{i\mu}^2} + \sum_{i=0}^{29} \sum_{\mu=x,y,z} V_M(Q_{i\mu} - Q_{i\mu}^{(0)}) + \frac{1}{2} \sum_{0 \leq i < j \leq 29} k_Z (Q_{iz} - Q_{jz})^2, \quad (28)$$

where  $Q_{i\mu}^{(0)}$  represents optimized geometry of the  $i$ -th surface atom and  $V_M(\rho)$  is a Morse potential with parameters  $D$  and  $a$ ,

$$V_M(\rho) = D[\exp(-2a\rho) - 2\exp(-a\rho)] \quad (29)$$

Such surface model has been used to study surface scattering dynamics of the CO/Cu(100) system<sup>37</sup>. One should note that the 3D CHO Hamiltonian  $\hat{H}_{3\text{D-CHO}}$  already contains the Hamiltonian for out-of-plane motion of the top atom and the coupling term between molecule and surface. Table V gives parameters of the present 98D Hamiltonian. Table VI gives numerical details of the present 98D ML-MCTDH calculations, where Figure 7 illustrates the multilayer tree-structure (called ML-tree) of the 98D wave function. We refer the reader to References<sup>23-25</sup> for further details on ML-MCTDH and ML-tree. By the present 98D ML-MCTDH calculations, one can find the phase shift as shown in Figure 8. This 98D results are similar to those of the low-dimensional models.

### C. Discussions on Experiments

It was found that<sup>38,39</sup> the fundamental CH<sub>3</sub> symmetric-stretching mode (called  $\nu_1$ ) and one of the first overtones of the CH<sub>3</sub> degenerate deformation mode (called  $\nu_5$ ) couple strongly via a Fermi interaction leading to two eigenstates splited by  $\sim 59 \text{ cm}^{-1}$ . This indicates existence of a pair of Fermi states of the CH<sub>3</sub> symmetric-stretching mode  $\nu_1$ , called  $\nu_1$ -I and  $\nu_1$ -II. These two eigenstates are linear combinations of two zero-order modes in symmetric and antisymmetric forms. Two Fermi-coupled vibrations execute synchronized motions in the  $\nu_1$ - $\nu_5$  space with comparable amplitudes, but differing in their relative phases. By their crossed-molecular-beam experiments, Pan and Liu<sup>11</sup> found Fermi-phase-induced interference phenomenon in the Cl + CH<sub>3</sub>D ( $\nu_1$ -I/ $\nu_1$ -II)  $\rightarrow$  CH<sub>2</sub>D ( $\nu = 0$ ) + HCl ( $\nu$ ) reaction and proposed nature of this phenomenon. First, this reaction has a late barrier with a product-like transition state (TS) in the exit channel which implies that the reactant needs appropriate motions to turn the corner toward the TS, as expected by Polanyi's rule<sup>17,18</sup>. Classically, for the in-phase  $\nu_1$ -I reagent, the CH<sub>3</sub>D molecule first stretches and bends,

then shrinks and straightens. In contrast, for the out-of-phase  $\nu_1$ -II, it is most likely to be found the  $\text{CH}_3\text{D}$  molecule either stretched and near planar, or squeezed and bent. Due to the multidimensional nature of the system, the corner-turning effects are of multiple folds. As  $\text{CH}_3\text{D}$  hits the corner-turning wall, the impulse may either act in concert or counteract the incoming Fermi-coupled vibrational motions. By such analysis based on classical-mechanical view, Pan and Liu<sup>11</sup> proposed that the prime factor to consider is how well the force vectors along the stretching and bending directions match with the in-phase or out-of-phase oscillation to allow the appropriate pathway towards the TS. By the present theory on the adiabatic and diabatic EOMs of Equations (17) and (18), it should be possible to interpret the above experiments by solve an appropriate EOM on coupled-vibrational system. For instance, separating strongly coupled modes, say  $\nu_1$  and  $\nu_5$ , from the other vibrational modes, one can construct the Hamiltonian model in Equation (4). Then, letting the  $\nu_1$ -I and  $\nu_1$ -II states be basis in Equation (12), one can obtain the EOMs of the other modes. By solving such matrix EOMs, we can explore how the  $\nu_1$ -I and  $\nu_1$ -II states influence the reaction dynamics of  $\text{Cl} + \text{CH}_3\text{D}$  ( $\nu_1$ -I/ $\nu_1$ -II). Such dynamics is non-adiabatic at the level of nuclear motions rather than that of electronic motions. Of course, the core questions of the above calculations are how to construct the Hamiltonian model and which EOM is adopted. These two questions are similar to those on electronic structure in non-adiabatic chemical dynamics.

Next, Beck and co-workers<sup>14</sup> reported several results by their experiments on  $\text{CH}_4/\text{Au}(111)$ . First of all, Beck and co-workers<sup>14</sup> found the implications of the strict magnetic quantum number conservation required for rovibrational state interference (RSI) channel suppression. Such state purity in the RSI-allowed levels was unobserved in molecule-surface scattering before this recently reported experiments. Moreover, rotation in the plane parallel to the surface must be strongly decoupled from the decohering influence of the surface phonons<sup>14</sup>. Obviously, this is consistent with previous theoretical calculation results obtained from the lattice effects on the adsorption dynamics of  $\text{CO}/\text{Cu}(100)$ <sup>15,19,37,40</sup>. Lastly, these experimental results<sup>14</sup> serve as a particularly cogent illustration of the role of symmetry. To explain the striking regularities in the experiments, Beck and co-workers<sup>14</sup> considered the existence of a continuous family of reflection symmetries in the polyatomic-molecule-surface interaction, where all of these symmetries are discrete in that their actions always in a finite change in the molecular coordinates. Due to the inapplicability of the Nöther theorem, discrete symmetries are confined to a limited role in a classical-mechanical context. However, the quantum-mechanical superposition elevates the role of reflections and other discrete symmetries. The high contrast interference phenomena<sup>14</sup> demonstrate that quantum ef-

fects are dominate even for complex molecular-surface scattering at room temperature.

Drawing inspiration from experiments reported by Yang and co-workers<sup>8</sup> and Beck and co-workers<sup>14</sup>, an ideal experiment as illustrated by Figure 9 is proposed to verify the sign change of the molecular wave function as indicated by Equation (16). To understand the quantum interference effects, Yang and co-workers<sup>8</sup> detected unusual oscillations in the differential cross section by measuring two topologically distinct pathways in the  $\text{H} + \text{HD} \rightarrow \text{H}_2 + \text{D}$  reaction. The notable oscillation patterns are attributed to the strong quantum interference between the direct abstraction pathway and an unusual roaming insertion pathway. Such interference pattern<sup>8</sup> also provides a sensitive probe of the geometric phase effect at an energy far below the conical intersection, clearly demonstrating the quantum nature of this reaction. The ideal experiment (see also Figure 9) can be carried out using a molecule-beam apparatus based on light molecule, say hydrogen or methane, which scatters from a metal surface, say gold, held at given surface temperature. A pump laser might be adopted for selecting rovibrational states of the molecule. The surface should be rotatable around the center of the scattering target region, so that possible to vary the incident angle  $\theta_{\text{ini}}$ . The scattered molecule was detected by a tagging laser combined with a bolometer detector to permit state-resolved population measurements of the scattered molecule. The incident angle and scattering angle  $\theta_{\text{fin}}$ , defined with respect to the surface normal, are independently variable. Time-of-flight (TOF) spectra at different incident angle may be further accumulated at the corresponding backward scattering direction. As illustrated by Figure 9, given the incident molecular wave function  $\varphi$ , the scattered and incident molecular wave functions superimpose to  $\varphi + \varphi'$ . Here,  $\varphi'$  means scattered wave function that depends on rotational coordinate of the surface atom  $\theta$ . In this process, both  $\theta_{\text{ini}}$  and  $\theta_{\text{fin}}$  are determined by rotation radius  $R_0$  of the surface atom, which is represented by  $\theta$ . Because of the phase shown by Equation (16), if there is no reaction and other transition one may observe that the intensity of molecular signal in the form

$$|\varphi + \varphi'|^2 = 2|\varphi|^2(1 + \cos \vartheta). \tag{30}$$

Since  $\varphi + \varphi'$  which should depend on  $\theta$ , by Equation (30) one can connect the phase  $\vartheta$  with experimental angle  $\theta$ .

#### D. Geometric Perspectives

The Berry phase effects on electronic properties<sup>4</sup> play a fundamental role in describing the geometric features as the parameters are varied. Similarly, the present work finds the Berry phase

effects on nuclear properties. Now, it is necessary to discuss this issue from the view of geometry. To this end, we should turn to the concept of Berry connection  $A_n(\mathfrak{z}) = i\langle\psi_n|\partial_{\mathfrak{z}}|\psi_n\rangle_q$  (see Equation (2)). One of examples is the NACM term in the adiabatic EOMs (see Equations (11) and (17)). In differential geometry, the concept of connection is introduced to compare vectors in nearby vector spaces enabling us to find whether the direction of a vector is changed when it parallel transports along a path (for example, the close path  $\Gamma$  in Equation (14)). The parallel transport does not change length and direction of the tangent vector of a geodesic, which can be seen as a “straight line” in curved manifolds. For example, in flat Euclidean space, a vector undergoing parallel transport along a straight line, *i.e.* geodesic, does not change its length or direction. Extending to flat Hilbert space, the adiabatic motion of the quantum state in it is a typical example of the parallel transport, where the norm and phase of the state remain invariant. In this case, the motion is unaffected by the slow variation of external parameters. Now, introducing the parameter space the flat space might become curved due to the changing external parameters. In this case, answering the question whether the direction of a vector is changed when it parallel transports along a close path can be used to figure out whether the space is curved. For example, parallel transport of a vector along a Möbius band results in a reversal of the vector orientation because the non-trivial monodromy of the band connection induces a  $\pi$ -rotation under parallel transport. Similar analysis on the Klein bottle can be given indicating parallel transport of a vector in the curved space. Its non-abelian holonomy could constrain wave function phase choices in low-dimensional systems. Turning to Equation (1), if the space is curved (by, for example, introducing parameter space as in the present theory), the quantum state is parallel transported along the curve path making its phase change. This leads to the Berry phase whose correspondence in geometry is the holonomy angle. In general, the holonomy angle quantifies the Berry phase accumulated by the wave function after parallel transport in parameter space. For a closed loop, this angle is determined by the integral of the Berry connection, as shown by Equations (2) and (3).

As shown in Section III B, the phase angle is changed by  $\pi$  at the critical point in the parameter space. Now, we should turn to the question where the phase angle will be changed. In the theory beyond the BOA, the electronic wave function changes its sign by adiabatically moving the molecular system (*i.e.* parallel transport of its quantum state) along the close path in the  $g$ - $h$  space around one CI point (see Section II B). If the close path encircles two CI points, however, the electronic wave function will not change its sign. This topological characteristic is usually quantified by a topological invariant, called Chern number, which characterizes certain properties

of phases in quantum systems. With the Berry connection  $A_n(\mathfrak{z})$  in Equation (2), the Chern number is defined as

$$C_n \propto \int_{\Gamma} d\mathfrak{z} (\partial_{\mathfrak{z}} \times A_n(\mathfrak{z})) = \int_{\Gamma} d\mathfrak{z} F_n(\mathfrak{z}), \quad (31)$$

where  $F_n(\mathfrak{z}) = \partial_{\mathfrak{z}} \times A_n(\mathfrak{z})$  is the Berry curvature for the  $n$ -th state. The integral of Equation (31) is taken over the parameter space along the path  $\Gamma$ . According to Equation (31), the Chern number counts the number of times the Berry curvature “wraps” around the parameter space and the number of the critical point. The latter gives the number of changing the sign of the wave function. Taking the Möbius band again as an example, an odd Chern number implies a Möbius strip-like twist in the bundle, causing the wave function to flip sign after traversing a loop. Therefore, if the Chern number is odd, the wave function changes sign; if even, it does not. In the present theory for nuclear evolution, the parameter space contains environmental conditions which vary slowly leading to the adiabatic evolution of the molecular system. The Chern number counts the number of the critical points, where the conditions of adiabatic evolution are broken. In Table VII, we collect the above geometric features of the Berry phase effects for both electron and nuclear, together with their relationships with the corresponding electromagnetic features, demonstrating that the critical point geometrically exhibits characteristics similar to those of charges. Therefore, the separation of the DOFs of the molecular system also leads to fruitful geometric characteristics, like those in electronic-structure theory, condensed matter physics, and field theory.

#### IV. CONCLUSIONS

In this work, the Berry phase effects of the nuclear wave function are found and discussed by considering the essence in separating reactant degrees of freedom (DOFs). The phase effects on electronic properties give rise to quantum interferences already observed by experiments<sup>9,14</sup>. In quantum dynamics calculations on high-dimensional reaction, dimensionality reduction is often employed to save computational cost. For instance, in constructing the PES of molecule-surface system and then propagating its wave function, the surface atoms are usually supposed to be fixed at their optimal conformation. In calculations on quantum state-resolved dynamics of a chemical reaction, reactants are usually prepared in separated eigenstates of individual fragments, and their direct-product is then evolved in time. In this work, we focus on the essence in separating them and the Berry phase effects of the nuclear wave function. By the present theory, mechanism of inter/intramolecular energy redistribution is developed to deeply understand reactive dynam-

ics with multivibrational states. To demonstrate the present theory, two three-dimensional (3D) models reductively describing the molecular reaction are developed to simulate transport of the system along a closed loop in a parameter space represented of inter/intramolecular energy transfers. Employing these models, extensive multiconfigurational time-dependent Hartree (MCTDH) calculations are performed to solve the time-dependent nuclear Schrödinger equation at various initial conditions. These calculations clearly indicate quantum interference in the parameter space. Discussions on the separation of the reactants are made, while perspectives on the Berry phase effects predicted by the present work are given from the viewpoint of differential geometry. As a conclusion remark, the Berry phase effects on molecular dynamics are also thoroughly compared with those on electronic properties and mode/bond-specific reactivity.

## ACKNOWLEDGEMENTS

The financial supports of National Natural Science Foundation of China (Grant No. 22273074) and Fundamental Research Funds for the Central Universities (Grant No. 2025JGZY34) are gratefully acknowledged. The authors also thank the *Centre National de la Recherche Scientifique* (CNRS) International Research Network (IRN) “MCTDH” which is a constructive platform for discussing quantum dynamics. The authors are grateful to Dr. C. S. Reilly (EPFL) and Prof. Dr. H.-D. Meyer (Heidelberg) for helpful discussions and also grateful to anonymous reviewers for their thoughtful suggestions.

TABLE I: Comparison of the present separation theory in molecular scattering (MS) with that in electron-nuclear (EN) system by several criteria (given in the second column). Both separation theories focus on dynamics of fast sub-systems, *i.e.*, motions along reaction coordinate and electronic motions in chemical reaction. The third and fourth columns give the characteristics of the MS and EN separations, respectively. The rightmost column gives remarks on corresponding comparison.

No.	Criteria	MS	EN	Remark
1	slow object	inactive fragments	nuclear	heavy part in the system <sup>a</sup>
2	fast object	active fragments	electron	light part in the system <sup>a</sup>
3	degeneracy space	parameter space	branching $g$ - $h$ space <sup>b</sup>	the degeneracy is lifted linearly
4	degeneracy object	motion and assignment	electronic energy	physical quantities degenerated in the degeneracy space
5	degeneracy topology	semi-conical intersection	conical intersection <sup>c</sup>	topology of the degeneracy object in the degeneracy space
6	phase	molecule <sup>d</sup>	electron <sup>d</sup>	see Equations (8) and (16)
7	coupling	mass coupling <sup>e</sup>	electromagnetic coupling <sup>f</sup>	in essence, mass coupling
8	adiabatic dynamics	molecular phase changed	electronic phase changed	invariant state of the fast object
9	diabatic dynamics	IMR/IVR process	electronic-state transition	multi-state transition of the fast object
10	non-adiabatic dynamics	IMR/IVR process	electronic-state transition	model coupling among states of the fast object

<sup>a</sup> According to Equations (7) and (11), eigen-energy values of slow and fast objects are  $\mu_1$  and  $E(\mathbf{Q})$ , respectively.

<sup>b</sup> The gradient difference  $g$  describes the gradient difference between the two electronic states, while the non-adiabatic coupling  $h$  describes the strength of coupling.

<sup>c</sup> The 2D CHO model predicts a semi-conical intersection topology as previously discussed<sup>15,19</sup>.

<sup>d</sup> If and only if the system moves along a closed loop in the parameter space, the wave function of the light part undergoes a phase change.

<sup>e</sup> Coupling between the molecule and surface is arisen from mass ratio between the molecule and surface.

<sup>f</sup> The Born-Oppenheimer approximation is arisen from electronic motions in the molecular system

TABLE II: Masses and parameters of the models used in the quantum dynamics calculations for demonstrating the present theory. The second, third, and fourth columns give masses (in dalton) of  $m_1$ ,  $m_2$ , and  $m_3$ , respectively. The fifth column gives the imitation of model, including  $\text{H} + \text{H}_2$ ,  $\text{H} + \text{OH}$ ,  $\text{CO}/\text{Cu}(100)$ , and  $\text{CH}_4/\text{Au}(111)$ . The sixth and seventh columns give values of  $\zeta_1$  and  $\zeta_2$  in the 3D CHO model (see Equation (20)), respectively. The eighth and ninth columns give values of  $\kappa_1$  and  $\kappa_2$  in the 3D REX model (see Equation (22)), respectively. The rightmost column gives remarks of the model.

No.	Mass models			Parameters				Remark	
	$m_1$	$m_2$	$m_3$	Imitation	$\zeta_1$	$\zeta_2$	$\kappa_1$		$\kappa_2$
1	1.000	1.000	1.000	$\text{H} + \text{H}_2$	1.000	1.000	0.125	0.125	the basic model
2	1.000	16.000	1.000	$\text{H} + \text{OH}$	0.250	4.000	$3.257 \times 10^{-3}$	0.443	dissociation of water
3	16.000	12.000	63.546	$\text{CO}/\text{Cu}(100)$	1.155	0.435	4.852	0.322	CO adsorbed on copper
4	15.000	1.000	196.967	$\text{CH}_4/\text{Au}(111)$	3.873	$7.125 \times 10^{-2}$	0.928	$3.557 \times 10^{-4}$	dissociative chemisorption of $\text{CH}_4$ on gold

TABLE III: Parameters in the present Hamiltonian models based on which the MCTDH calculations are performed to illustrate the wave function phase. The upper panel gives the model for the molecule-surface system, while the lower panel gives the model for the chemical reaction. The second column gives the parameters in defining the present demonstration models. The third column gives values of the parameters in the present calculations. The frequency parameters  $\eta$  and  $\xi$  of the 3D CHO model represent states of the reactants, such as the nozzle and target temperatures. The frequency parameters  $\alpha$  and  $\beta$  of the 3D REX model represent internal motions of the reactant fragments revised by the H + H<sub>2</sub> system. The  $V_3$  term in  $V_{3D-REX}$  is adopted by the BKMP2 PES of the H + H<sub>2</sub> system<sup>20</sup>, while the  $V_{rev}$  term is a perturbation of  $V_3$ . As usual, the atomic units are used. The fourth column gives expression in which the parameter appear. The rightmost column gives remarks on these parameters.

No.	Parameter	Value	Expression	Remark
<i>Parameters of the Hamiltonian model for surface scattering</i>				
1	$m_1$	— <sup>a</sup>	Equation (20)	mass of the atom in molecule
2	$m_2$	— <sup>a</sup>	Equation (20)	mass of the atom in molecule
3	$m_3$	— <sup>a</sup>	Equation (20)	mass of surface atom
4	$\omega_2$	500.0 cm <sup>-1</sup> <sup>b</sup>	Equation (20)	force constant of the adsorption
5	$\eta$	$\omega_1^2/\omega_2^2$	Equation (20)	function of nozzle temperature
6	$\xi$	$\omega_3^2/\omega_2^2$	Equation (20)	function of target temperature
<i>Parameters of the Hamiltonian model for molecular reaction</i>				
1	$m_1$	— <sup>a</sup>	Equation (22)	mass of the fragment #1, the colliding group
2	$m_2$	— <sup>a</sup>	Equation (22)	mass of the fragment #2 in the target group
3	$m_3$	— <sup>a</sup>	Equation (22)	mass of the fragment #3 in the target group
4	$\omega_{23}$	1.0 cm <sup>-1</sup> <sup>c</sup>	Equation (23)	force constant of target bonding
5	$\alpha$	$\omega_{12}^2/\omega_{23}^2$	Equation (23)	internal motions of fragments #1 and #2
6	$\beta$	$\omega_{13}^2/\omega_{23}^2$	Equation (23)	internal motions of fragments #1 and #3

<sup>a</sup> See Table II for various models.

<sup>b</sup> It is a typical frequency value for restricted vibration of the entire adsorbed molecule.

<sup>c</sup> The value should ensure that the additional term  $V_{rev}$  of Equation (21) is small enough and thus a perturbation.

TABLE IV: DVR-grids used in the present quantum dynamics calculations, and parameters of the initial guess function for preparing the initial wave function  $\Psi(t=0)$ . The definitions of the surface geometry and coordinates (indicated in the first column) are given in Figure 1. The second column describes the primitive basis functions, which underlay the DVR. The third column gives the number of the grid points. The fourth column gives the range of the grids in atomic unit or radian. The fifth column gives the symbol of the one-dimensional (1D) function for each coordinate of the guess function. The initial wave function is then computed by relexing the guess function. The other columns give the parameters for these 1D functions, including positions and momenta in the 1D function, frequency ( $\omega_{\text{HO}}$ ) and mass ( $M_{\text{HO}}$ ) of the harmonic oscillator (HO) function, width of the Gaussian function (*i.e.*, and variance of the modulus-square of the Gaussian function,  $W_{\text{GAUSS}}$ ).

Coordinates	Primitive basis function			Initial guess function			
	Symbol <sup>a</sup>	Grid points	Range of the grids	Symbol <sup>b</sup>	Position	Momentum	Parameters
<i>Coordinates of the molecule-surface model</i>							
$q_1$	HO	15	[-0.800, 0.800]	HO	0.0	0.0	$500.0 \text{ cm}^{-1}, m_1$
$q_2$	HO	15	[-0.800, 0.800]	HO	0.0	0.0	$500.0 \text{ cm}^{-1}, m_2$
$q_3$	HO	15	[-0.800, 0.800]	HO	0.0	0.0	$500.0 \text{ cm}^{-1}, m_3$
$\eta$	SIN	68	[0.00, 2.50]	GAUSS	1.5	-15.0	$W_{\text{GAUSS}} = 0.12$
$\xi$	SIN	68	[0.00, 2.50]	GAUSS	1.5	-15.0	$W_{\text{GAUSS}} = 0.12$
<i>Coordinates of the reaction model</i>							
$r_d$	SIN	68	[1.00, 9.04]	GAUSS	4.5	-8.0	$W_{\text{GAUSS}} = 0.25$
$r_v$	SIN	48	[0.60, 6.24]	EIGENF <sup>c</sup>	—	—	ground state
$\theta$	LEG	31	[0, $\pi$ ]	LEG	—	—	$j_{\text{ini}} = 0$
$\alpha$	SIN	68	[0.00, 2.50]	GAUSS	1.5	-15.0	$W_{\text{GAUSS}} = 0.12$
$\beta$	SIN	68	[0.00, 2.50]	GAUSS	1.5	-15.0	$W_{\text{GAUSS}} = 0.12$

<sup>a</sup> Symbols HO and SIN stand the harmonic oscillator and the sine DVR basis functions, respectively, while LEG denotes a one-dimensional Legendre DVR basis.

<sup>b</sup> Symbols HO and GAUSS designate the harmonic oscillator eigenfunction and Gaussian function, respectively, while LEG denotes the Legendre function.

<sup>c</sup> Symbol EIGENF means the eigenfunction of a specified potential which, in this work, is the potential energy of the H<sub>2</sub> molecule.

TABLE V: Same as Table III except for parameters in the present 98D Hamiltonian model for the molecule-surface system. Parameters of  $\hat{H}'_{\text{surf}}$  given in Equations (28) and (29) were previously optimized for the Cu(100) surface<sup>37</sup>.

No.	Parameter	Value	Expression	Remark
1	$m_1$	16.000 dalton	Equation (20)	mass of the atom in molecule
2	$m_2$	12.000 dalton	Equation (20)	mass of the atom in molecule
3	$m_3$	63.546 dalton	Equation (20)	mass of surface atom
4	$\omega_2$	500.0 cm <sup>-1</sup> <sup>a</sup>	Equation (20)	force constant of the adsorption
5	$\eta$	$\omega_1^2/\omega_2^2$	Equation (20)	function of nozzle temperature
6	$\xi$	$\omega_3^2/\omega_2^2$	Equation (20)	function of surface temperature
7	$k_b$	1000.0 cm <sup>-1</sup> <sup>a</sup>	Equation (27)	force constant of the bond
8	$k_R$	$1.000 \times 10^{-2}$ hartree	Equation (27)	force constant along the $R$ coordinate
9	$b_0$	2.267 bohr	Equation (27)	bond length
10	$R_0$	0.397 bohr	Equation (27)	radius of the closed loop
11	$\{Q_{i\mu}^{(0)}\}_{i=0}^{29}, \mu = x, y, z$	See Figure 6	Equation (28)	optimized coordinates of the $i$ -th atom
12	$d$	4.830 bohr	Equation (28)	lattice constant
13	$k_Z$	$1.100 \times 10^{-2}$ hartree	Equation (28)	coupling strength the non-top atoms
14	$D$	0.300 hartree	Equation (29)	deep of the Morse potential
15	$a$	0.390 Å <sup>-1</sup>	Equation (29)	width parameter of Morse well

<sup>a</sup> It is a typical frequency value for restricted vibration of the entire adsorbed molecule or bonding stretch.

TABLE VI: Same as Table IV except for the present 98D Hamiltonian model for the molecule-surface system. The atomic arrangement is shown by Figure 6. Parameters of the 98D Hamiltonian model is given in Table V. The sizes of the DVR basis functions are also given in Figure 7.

Coordinates	Primitive basis function			Initial guess function				
	Symbol <sup>a</sup>	Grid points	Position <sup>b</sup>	Parameters	Symbol <sup>c</sup>	Position <sup>b</sup>	Momentum	Parameters
$b$	HO	15	2.267 bohr	1000.0 cm <sup>-1</sup> , 6.857 dalton	HO	2.267 bohr	0.0	1000.0 cm <sup>-1</sup> , 6.857 dalton
$\chi$	PLEG <sup>d</sup>	15	—	$\chi \in [0, \pi]$	KLEG <sup>e</sup>	0.0	0.0	nosym <sup>f</sup>
$\phi$	EXP <sup>d</sup>	15	—	$\phi \in [0, 2\pi]$	K <sup>e</sup>	0.0	0.0	0 <sup>g</sup>
$z$	HO	15	2.835 bohr	500.0 cm <sup>-1</sup> , 28.0 dalton	HO	2.835 bohr	0.0	500.0 cm <sup>-1</sup> , 1.0 dalton
$R$	HO	15	0.397 bohr	10 <sup>-2</sup> hartree, 28.0 dalton	HO	0.397 bohr	0.0	10 <sup>-2</sup> hartree, 28.0 dalton
$\vartheta$	LEG	9	—	$\varphi \in [0, 2\pi]$	GAUSS	0.0	0.0	$W_{\text{GAUSS}} = 0.12$
$\eta$	SIN	15	—	$\eta \in [0.00, 2.50]$	GAUSS	1.5	-15.0	$W_{\text{GAUSS}} = 0.12$
$\xi$	SIN	15	—	$\xi \in [0.00, 2.50]$	GAUSS	1.5	-15.0	$W_{\text{GAUSS}} = 0.12$
$Q_{0x}$	HO	15	$Q_{0x}^{(0)}$	500.0 cm <sup>-1</sup> , 63.546 dalton	HO	$Q_{0x}^{(0)}$	0.0	500.0 cm <sup>-1</sup> , 63.546 dalton
$Q_{0y}$	HO	15	$Q_{0y}^{(0)}$	500.0 cm <sup>-1</sup> , 63.546 dalton	HO	$Q_{0y}^{(0)}$	0.0	500.0 cm <sup>-1</sup> , 63.546 dalton
$Q_{0z}$	HO	15	$Q_{0z}^{(0)}$	500.0 cm <sup>-1</sup> , 63.546 dalton	HO	$Q_{0z}^{(0)}$	0.0	500.0 cm <sup>-1</sup> , 63.546 dalton
$\{Q_{i\mu}^{(0)}\}_{i=1}^8, \mu = x, y, z$	HO	10	$\{Q_{i\mu}^{(0)}\}_{i=1}^8$	500.0 cm <sup>-1</sup> , 63.546 dalton	HO	$\{Q_{i\mu}^{(0)}\}_{i=1}^8$	0.0	500.0 cm <sup>-1</sup> , 63.546 dalton
$\{Q_{i\mu}^{(0)}\}_{i=9}^{20}, \mu = x, y, z$	HO	7	$\{Q_{i\mu}^{(0)}\}_{i=9}^{20}$	500.0 cm <sup>-1</sup> , 63.546 dalton	HO	$\{Q_{i\mu}^{(0)}\}_{i=9}^{20}$	0.0	500.0 cm <sup>-1</sup> , 63.546 dalton
$\{Q_{i\mu}^{(0)}\}_{i=21}^{29}, \mu = x, y$	HO	5	$\{Q_{i\mu}^{(0)}\}_{i=21}^{29}$	500.0 cm <sup>-1</sup> , 63.546 dalton	HO	$\{Q_{i\mu}^{(0)}\}_{i=21}^{29}$	0.0	500.0 cm <sup>-1</sup> , 63.546 dalton
$\{Q_{iz}^{(0)}\}_{i=21}^{29}$	HO	7	$\{Q_{iz}^{(0)}\}_{i=21}^{29}$	500.0 cm <sup>-1</sup> , 63.546 dalton	HO	$\{Q_{iz}^{(0)}\}_{i=21}^{29}$	0.0	500.0 cm <sup>-1</sup> , 63.546 dalton

<sup>a</sup> Symbols HO and SIN stand the harmonic oscillator and the sine DVR basis functions, respectively, while LEG denotes a one-dimensional Legendre DVR basis.

<sup>b</sup> Positions of the surface atoms,  $\{Q_{i\mu}^{(0)}\}_{i=0}^{29}, \mu = x, y, z$ , are illustrated in Figure 6 and can be computed by parameter  $d = 4.830$  bohr, as given in Table V.

<sup>c</sup> Symbols HO and GAUSS designate the harmonic oscillator eigenfunction and Gaussian function, respectively, while LEG denotes the Legendre function.

<sup>d</sup> Symbols PLEG and EXP denote two-dimensional Legendre and exponential DVR basis functions, respectively.

<sup>e</sup> Symbols KLEG and K denote associated Legendre polynomial and body-fixed magnetic quantum number, respectively.

<sup>f</sup> It means that no symmetry is set, that is all angle quantum number values are used.

<sup>g</sup> It means that body-fixed magnetic quantum number of initial wave function is zero.

TABLE VII: Comparisons of the concepts in the Berry phase effects on the nuclear and electronic properties, together with these concepts associated with electromagnetic (EM) field. The second column provides geometric concepts that will be compared to various fields. These concepts are the Berry connection, Berry curvature, and Berry phase, which arise in the parameter space. The third and fourth columns list physical insights of these concepts for the nuclear and electronic properties. The fifth column lists the electromagnetic quantities or properties associated with the geometric features. The rightmost column gives remarks of these physical quantities or geometric properties.

No.	Feature <sup>a</sup>	Nuclear	Electron	EM field	Remarks
1	connection	$A_n(\mathbf{z})$ in Equation (2)	diagonal element of electronic NACM <sup>c</sup>	analogous to the vector potential <sup>b</sup>	a gauge-dependent object encoding system's dependence on the parameters space
2	curvature	$F_n(\mathbf{z})$ in Equation (31)	curl of $\tau_{nm}^{\text{elec}}(\mathbf{y})$ <sup>d</sup>	effective magnetic field in parameter space <sup>b</sup>	a local geometric property of parameter space encoding the states' anholonomy under adiabatic parameter variations
3	phase	nuclear wave function	electronic wave function	geometric properties in both classical polarization dynamics and quantum photonic system	geometric properties of wave eigenstates
4	Chern number	number of critical points	number of CI points	global properties of EM modes <sup>e</sup>	a topological invariant classifying the global topology of the system's eigenstate bundle

<sup>a</sup> For clarity, the term "Berry" is omitted for the Berry connection, Berry curvature, and Berry phase.

<sup>b</sup> It is a concept in differential geometry but has similar expression to the corresponding concepts in the classical EM field leading to analogous phenomena.

<sup>c</sup> If the  $j$ -th electronic state  $v_j(\mathbf{x}, \mathbf{y})$  depends on electronic coordinates  $\mathbf{x}$  and parameters  $\mathbf{y}$ , the elements of the electronic NACM satisfy  $\tau_{jj}^{\text{elec}}(\mathbf{y}) = \langle v_j | \nabla_{\mathbf{y}} | v_j \rangle_{\mathbf{x}}$ .

<sup>d</sup> The Berry curvature of the  $n$ -th electronic state is  $\Omega_n(\mathbf{y}) = \nabla_{\mathbf{y}} \times \tau_{nn}^{\text{elec}}(\mathbf{y})$ . See also Footnote <sup>c</sup>.

<sup>e</sup> In general, the EM modes are defined for photons, or more precisely bosons, such as photon bands in periodic structures.

## FIGURE CAPTIONS

**Figure 1:** A cartoon of the 3D CHO models, together with eigenvalues degeneracy seams of the 3D CHO model at different mass parameters, where  $m_1$ ,  $m_2$ , and  $m_3$  denote the masses of the three atoms while  $\omega_1$ ,  $\omega_2$ , and  $\omega_3$  denote associated frequencies.

**Figure 2:** 2D surface plots and contour plots of  $V_{3D-REX}$  at (a)  $\theta = 0.0$ , (b)  $\theta = \pi/4$ , and (c)  $\theta = \pi/2$ , where the parameters are given in Table III and the masses are all 1.0 dalton. The two axes of the horizontal plane are  $r_d$  and  $r_v$ , and the vertical axis represents potential energy (in eV). The surface and contour plots are displayed in the upper and lower panels, respectively, in each subfigure. All of plots are computed at  $\alpha = \beta = 1$ .

**Figure 3:** Time-dependent phases (in radian) of the nuclear wave functions computed by the present MCTDH calculations through (a) the 3D CHO model and (b) the 3D REX model, where initial conditions and parameters are set to simulate different molecular systems. The black, red, blue, and green lines represent the phase angle of CO/Cu, HCH<sub>3</sub>/Au, H<sub>2</sub>O, and H + H<sub>2</sub>, respectively. The horizontal axis represents propagation time (in fs), the vertical axis indicates the phase angle.

**Figure 4:** Time-dependent phases (in radian) of the nuclear wave functions computed by the present MCTDH calculations through the 3D CHO model, where initial conditions and parameters are set to simulate different molecular systems, including (a) CO/Cu, (b) HCH<sub>3</sub>/Au, (c) H<sub>2</sub>O, and (d) H + H<sub>2</sub>. The horizontal axis represents propagation time (in fs), the left vertical axis indicates the phase angle (in radian), and the right vertical axis (in red words) shows the time-dependent expectation of  $\eta$ . The parameters of the 3D CHO model are given in Tables II and III. For clarity, in each subfigure we show only the time period in which the phase changes. In each subfigure, the black circles represent the time-dependent phase values (referred to the left axis). The red line represent the time-dependent expectation  $\langle \eta \rangle(t) = \langle \Psi(t) | \eta | \Psi(t) \rangle / \langle \Psi(t) | \Psi(t) \rangle$  (referred to the right axis). The blue symbol  $\times$  means the critical point  $\eta_c = \sqrt{1 + m_1 / \max(m_2, m_3)}$  (referred to the

right axis), where the phase should change.

**Figure 5:** Same as Figure 4 except for the 3D REX model, which is adopted to model scattering processes of (a) CO/Cu, (b) HCH<sub>3</sub>/Au, c) H<sub>2</sub>O, and (d) H + H<sub>2</sub>. Moreover, since the time-dependent phase of H + H<sub>2</sub> changes dramatically, one cannot clearly find transition of the phase angle and thus the time where the critical point  $\sqrt{2}$  occurs. For clarity, the critical point is shown by a blue dashed line in subfigure (d).

**Figure 6:** Geometry of the Cu(100) surface in the numerical demonstration on the present theory in surface scattering. At each the first and third layers of the model surface, a total of nine surface atoms are uniformly distributed across a  $3 \times 3$  grid layout and represent by black circles, while the atoms of the second layer are given by symbols  $\times$ . The center-of-mass (COM) of the molecule is represented by red circle. The surface plane is the  $x$ - $y$  plane and hence the original point is set at the top atom, denoted by #0. Moreover, the surrounding atoms at the first layer are sequentially numbered #1 through #8 in a clockwise arrangement centered on atom #0. The  $x$  and  $y$  axes are defined by the #0-#4 and #0-#2 connections, respectively. The molecular COM is described by  $\{R, \vartheta, z\}$ , where  $R$  denotes the radial distance from the origin to the projected point of the molecule and  $\vartheta$  represents the polar angle of this projected point. The chemical bonding between the surface atoms is governed by the Morse potential. The distance between adjacent surface atoms is denoted by  $d$ . By the same Morse potential, all of the surface atoms are fixed at solid surface along negative  $z$ - and lateral-directions.

**Figure 7:** The ML-MCTDH wave function structure (called ML-tree structure) for the present 98D calculations based on the Hamiltonian model given in Table III. The maximum depth of the ML-tree is six layers, and the first layer separates the molecular coordinates from those of the surface atoms, as shown in Figure 6. The number of SPFs are also given. The numbers of primitive basis sets to represent SPFs of the deepest layer are given next to the lines connecting with the squares (see also Table IV). For simple, subfigure (a) only shows the first 35 coordinates, while subfigure (b) shows the other 63 coordinates that should locate at the ML-tree structure in

the red box of subfigure (a).

**Figure 8:** Same as Figure 4 except for the 98D CHO model, which is adopted to model scattering processes of CO/Cu. The atomic arrangement and the ML-tree of the 98D wave function are given in Figures 6 and 7, respectively.

**Figure 9:** Ideal experiment to verify the sign change of the molecular wave function as indicated by Equation (16), drawn inspiration from experiments reported by Yang and co-workers<sup>8</sup> and Beck and co-workers<sup>14</sup>. It can be carried out using a molecule-beam apparatus based on rather light molecule, say hydrogen or methane, which scatters from a metal surface, say gold, held at given surface temperature. A pump laser should be adopted for selecting rovibrational states of the molecule. The surface should be rotatable around the center of the scattering target region, so that possible to vary the incident angle. The scattered molecule was detected by a tagging laser combined with a bolometer detector to permit state-resolved population measurements of the scattered molecule. The incident angle and scattering angle, defined with respect to the surface normal, are independently variable.

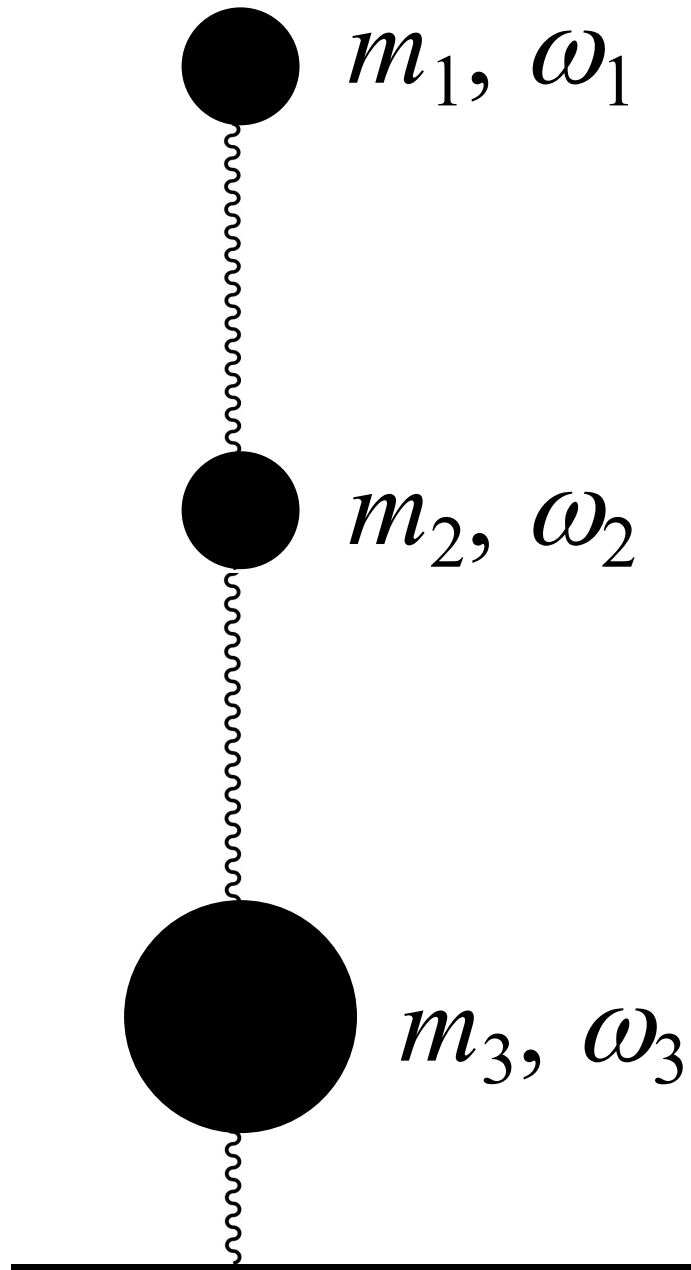
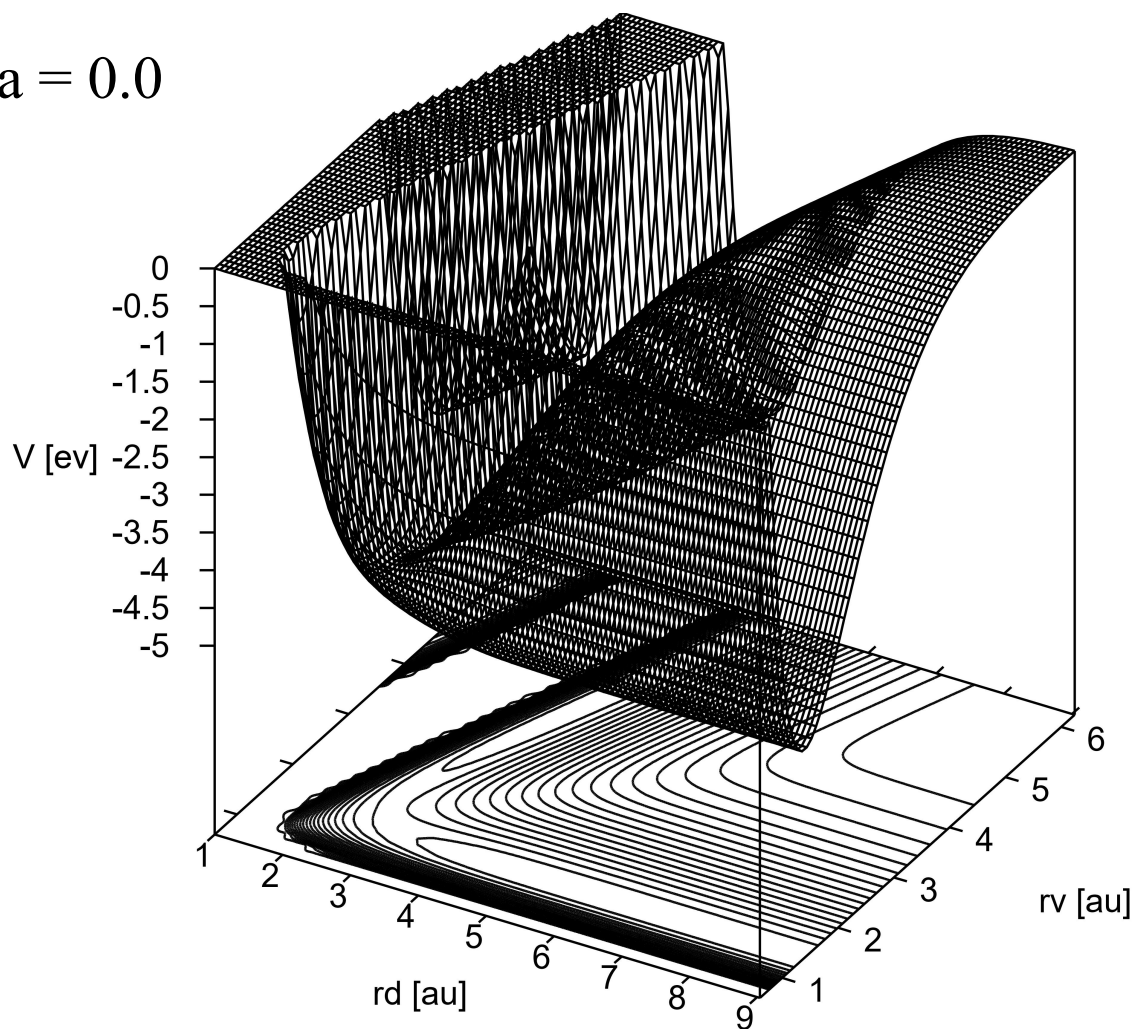


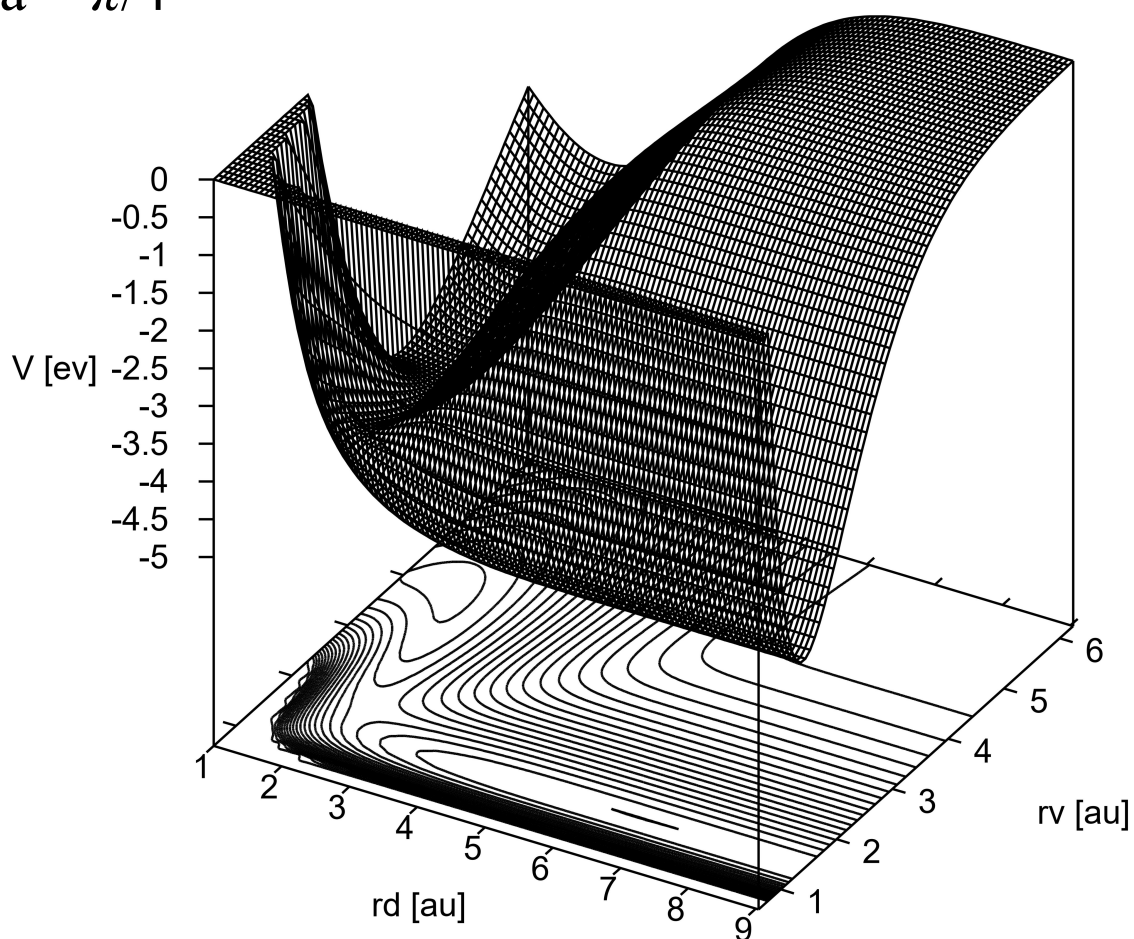
FIG. 1: Phase Expert, Meng

(a)  $\theta = 0.0$



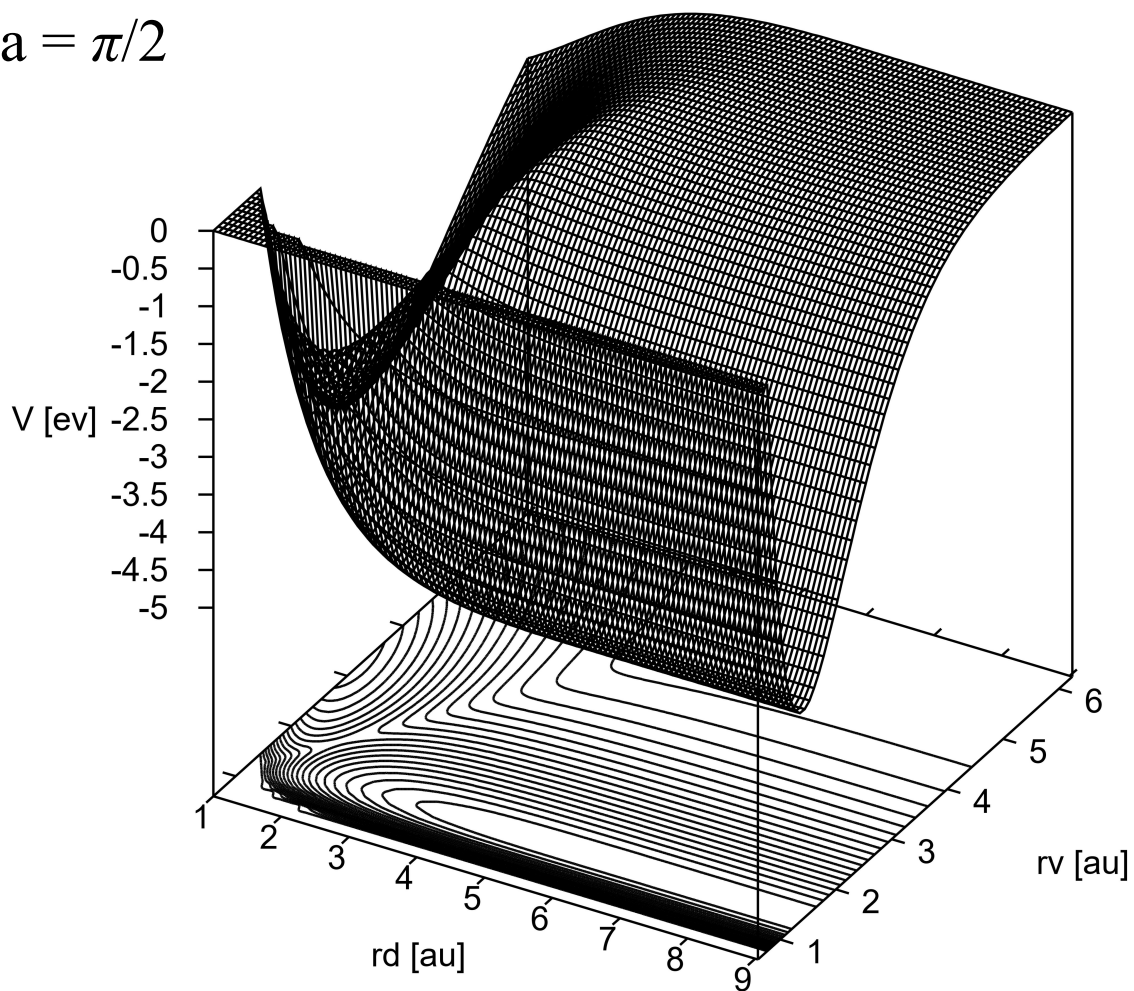
(a) Surface plot and contour plots of the PES for the 3D REX model at  $\theta = 0.0$

(b)  $\theta = \pi/4$



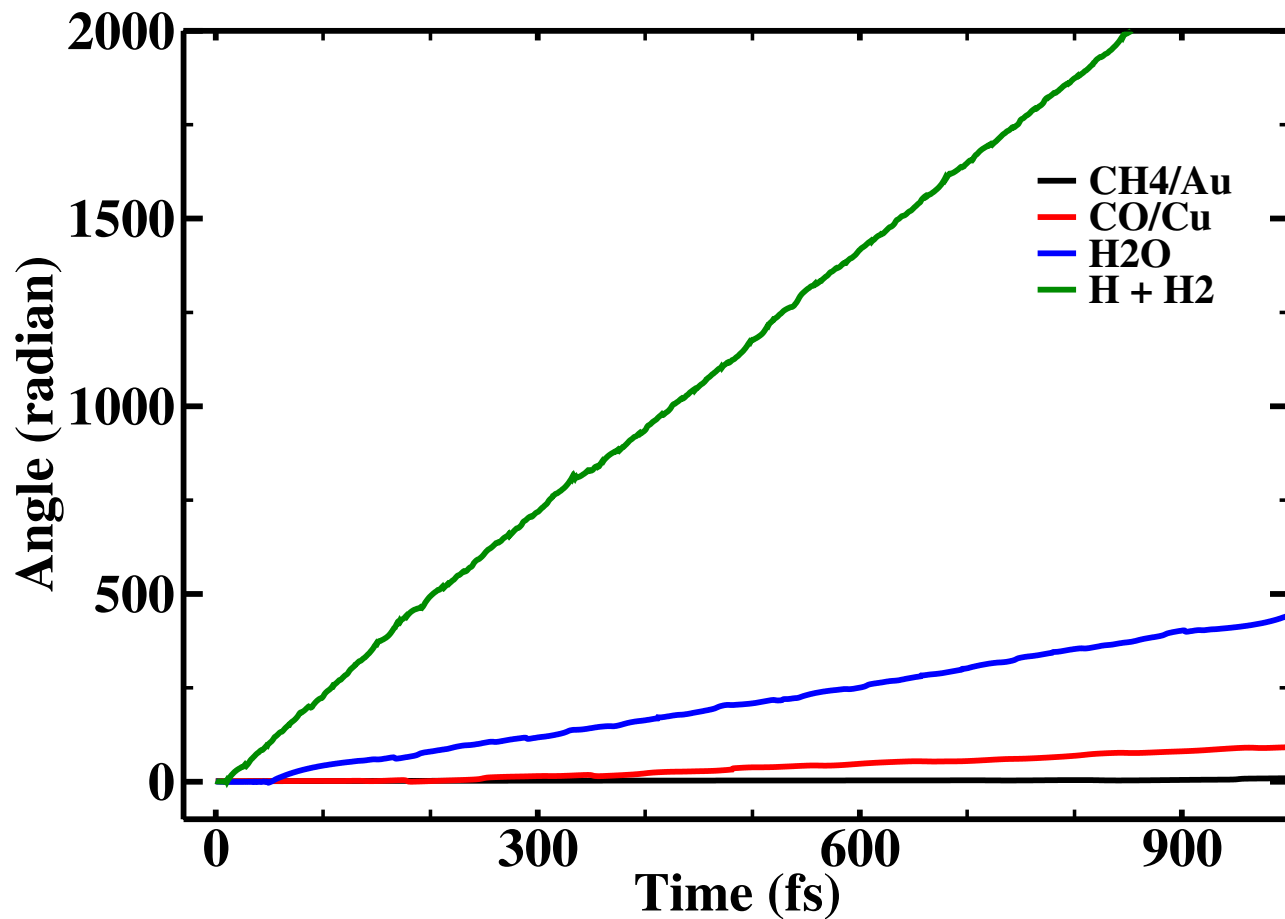
(b) Surface plot and contour plots of the PES for the 3D REX model at  $\theta = \pi/4$

(c)  $\theta = \pi/2$

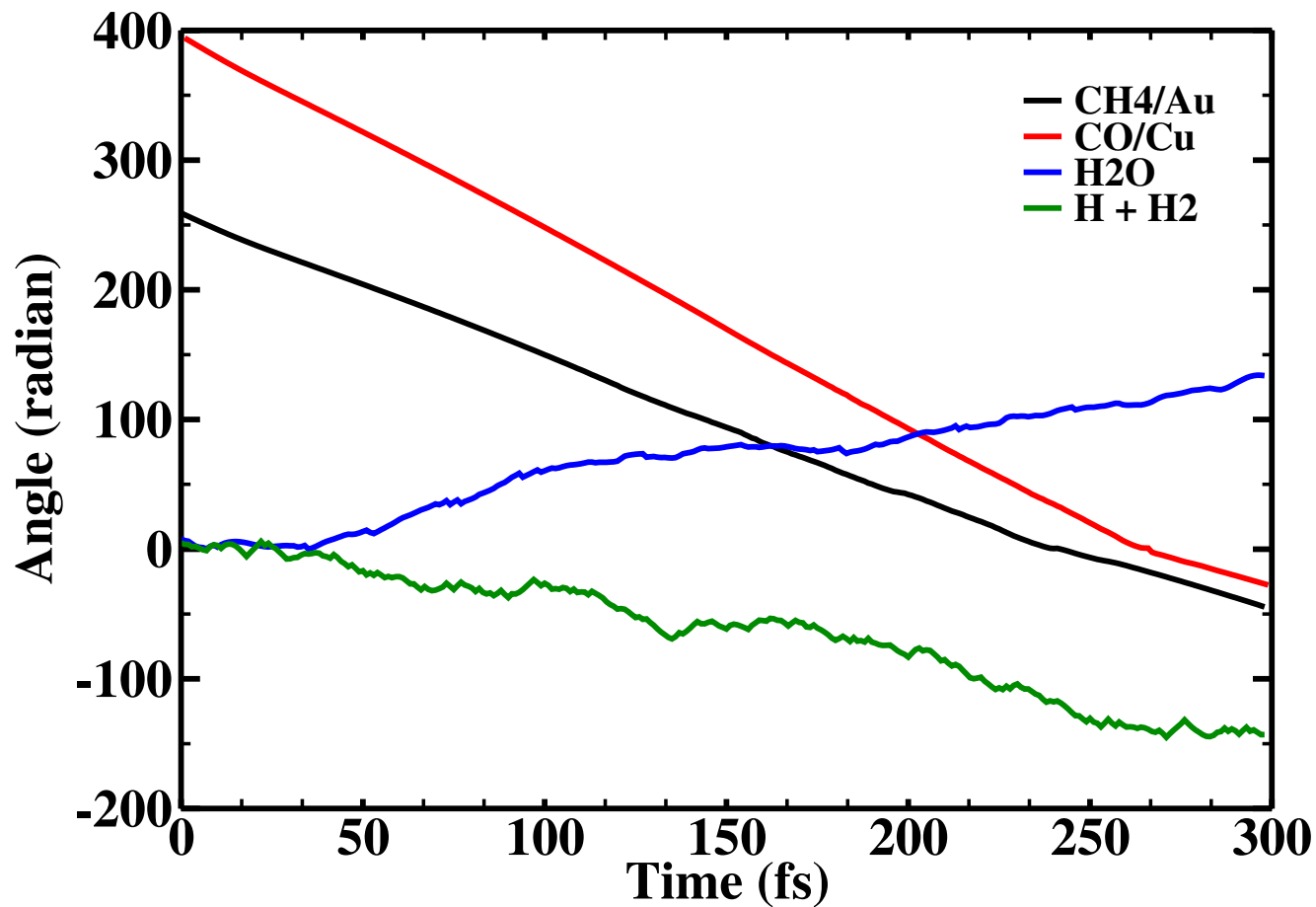


(c) Surface plot and contour plots of the PES for the 3D REX model at  $\theta = \pi/2$

FIG. 2: Phase Expert, Meng

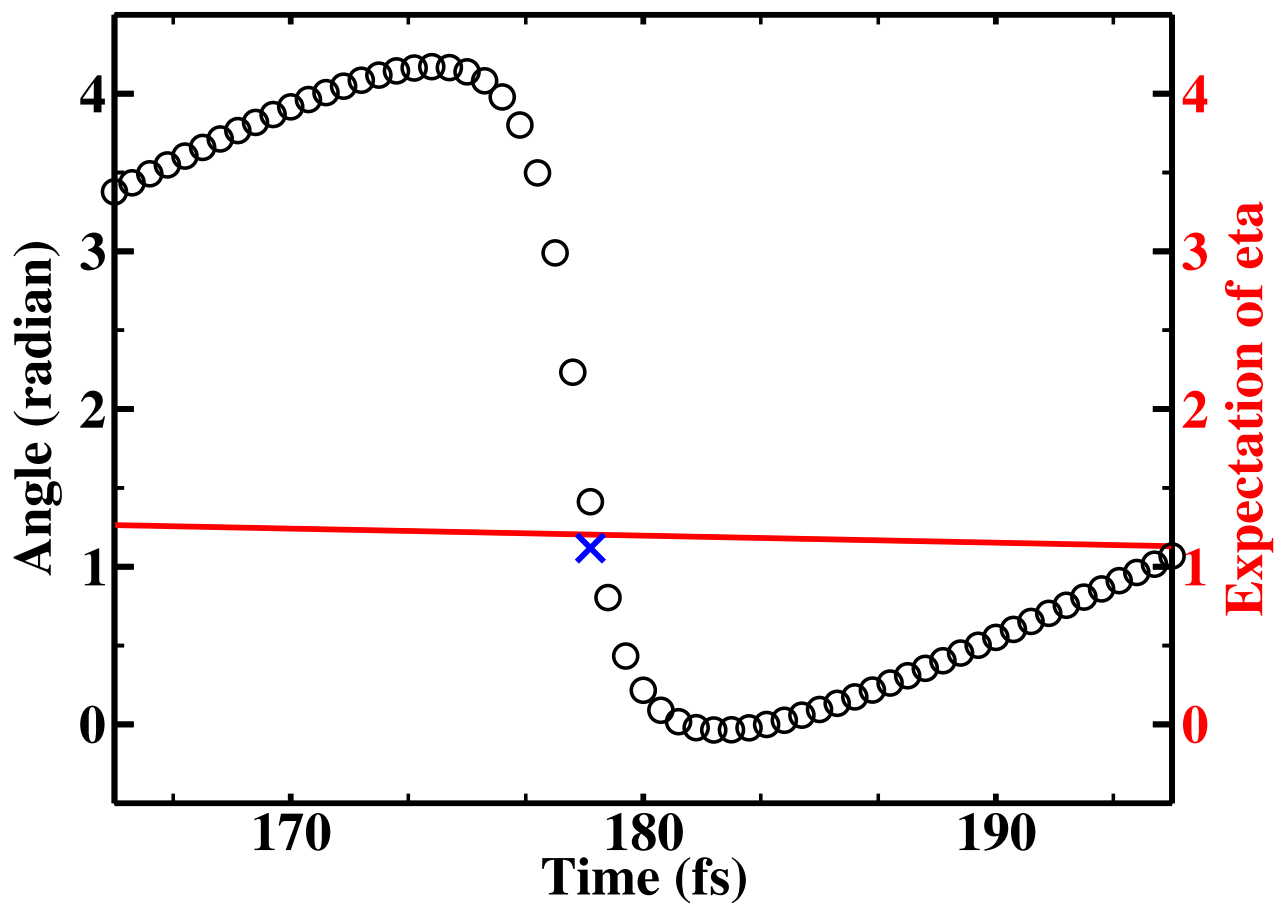


(a) Phase angle of the 3D CHO model

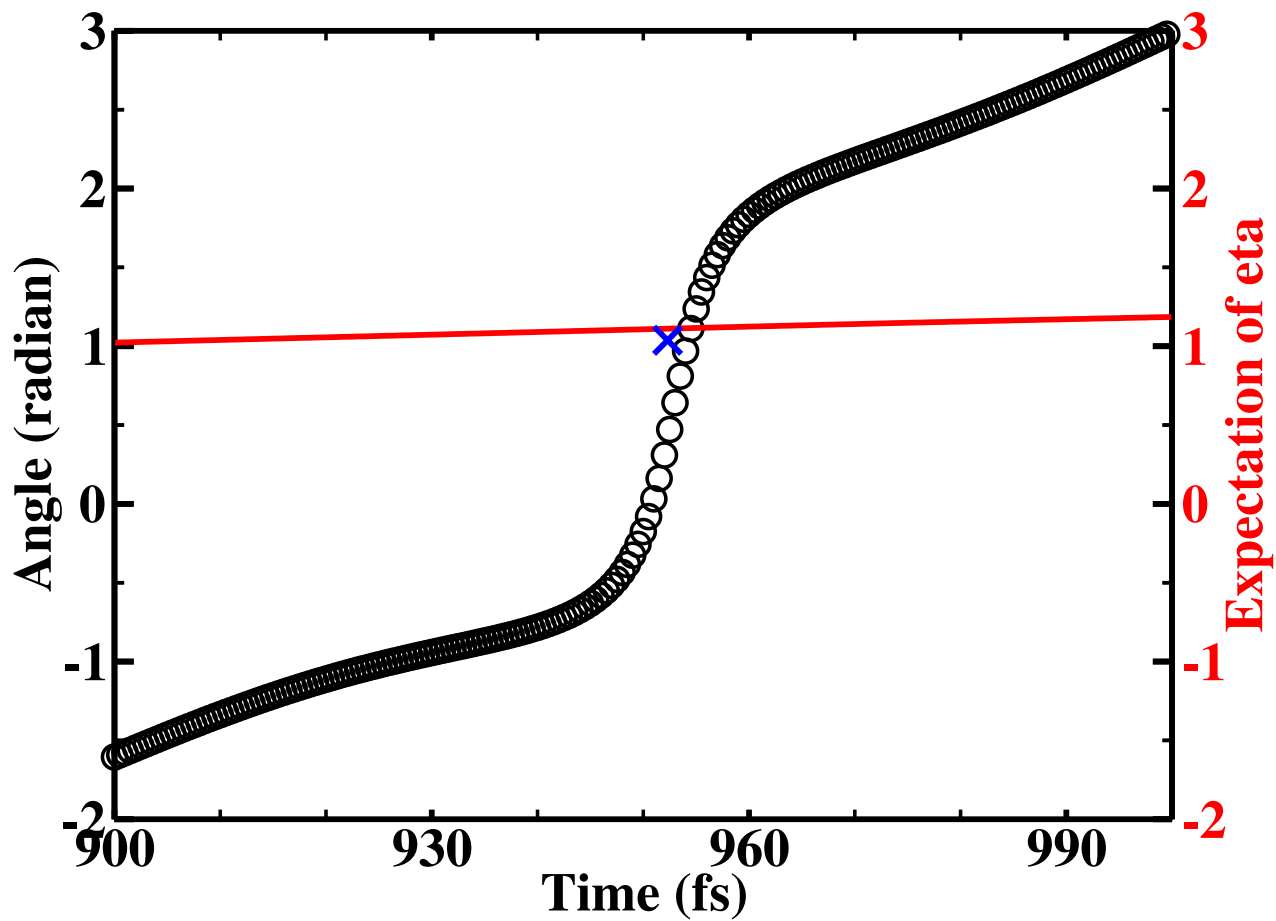


(b) Phase angle of the 3D REX model

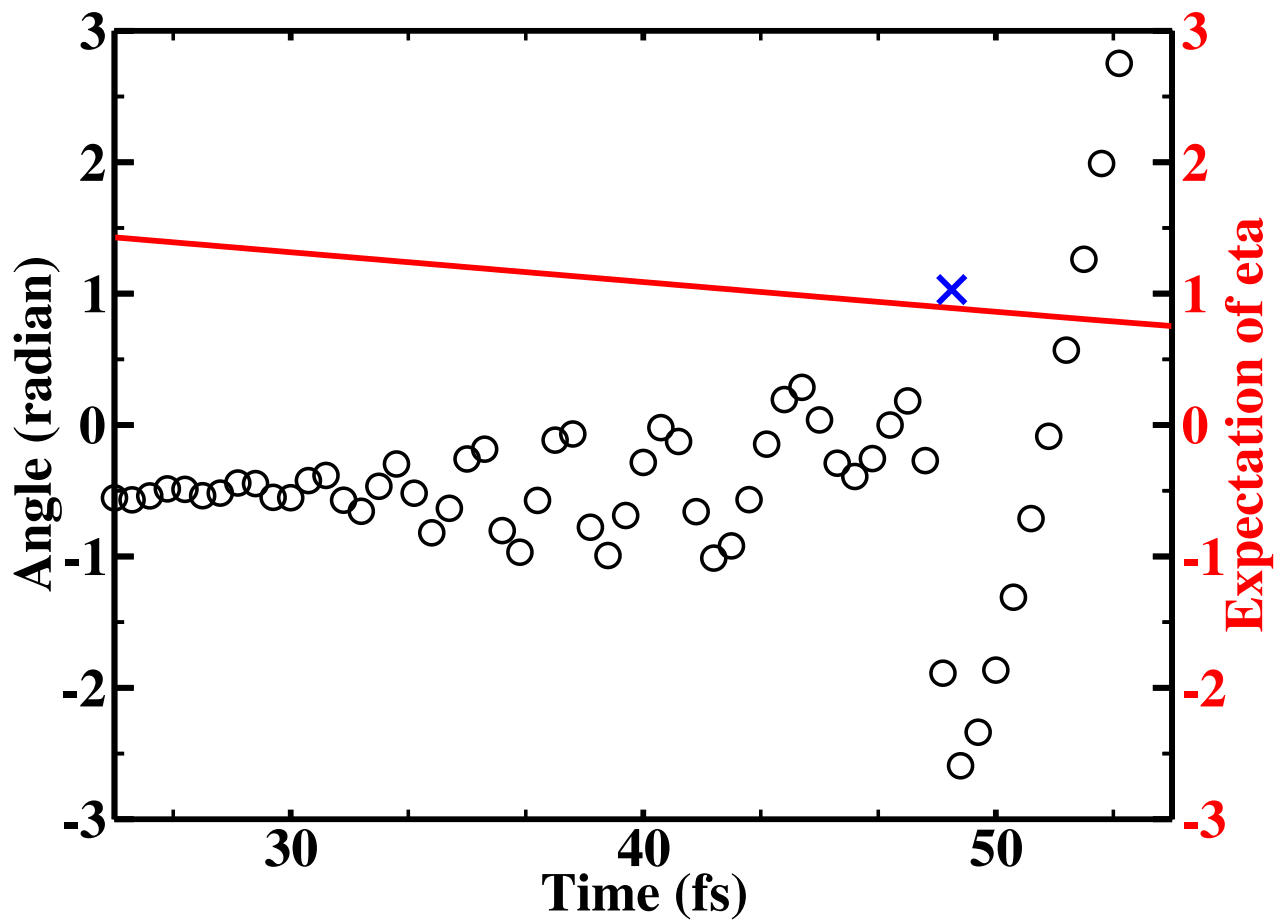
FIG. 3: Phase Expert, Meng



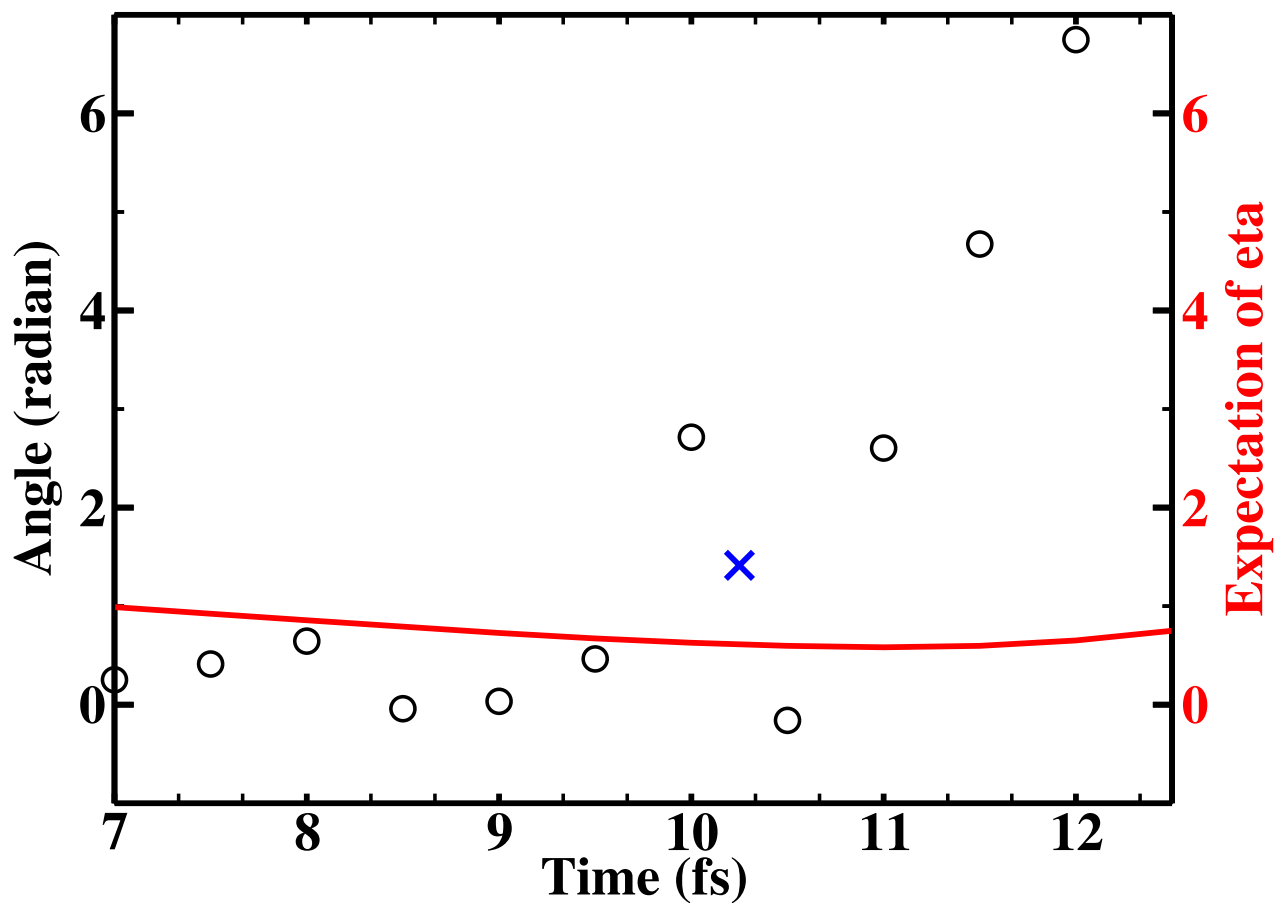
(a) Time-dependent phase of the 3D CHO model for CO/Cu



(b) Time-dependent phase of the 3D CHO model for CH<sub>4</sub>/Au

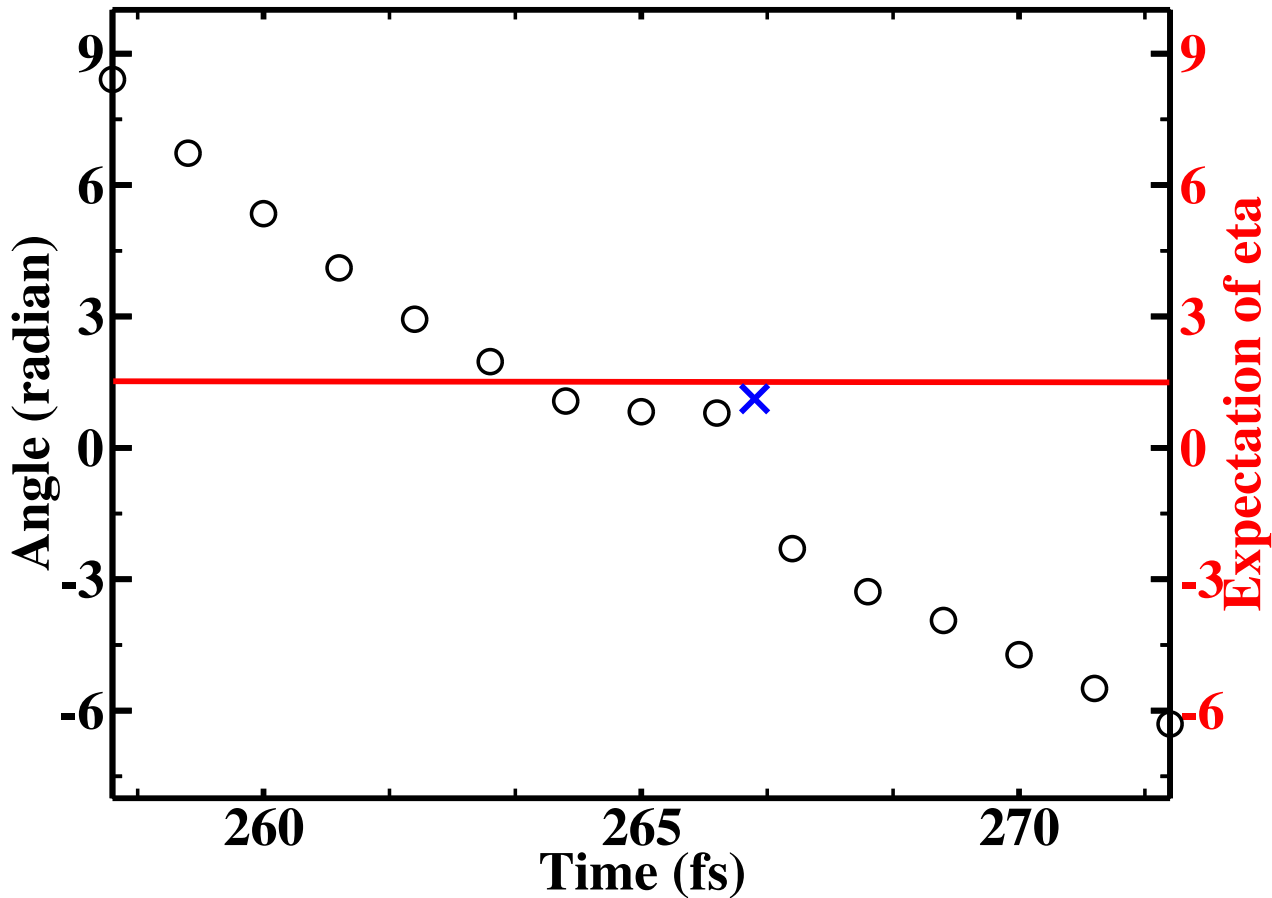


(c) Time-dependent phase of the 3D CHO model for H<sub>2</sub>O

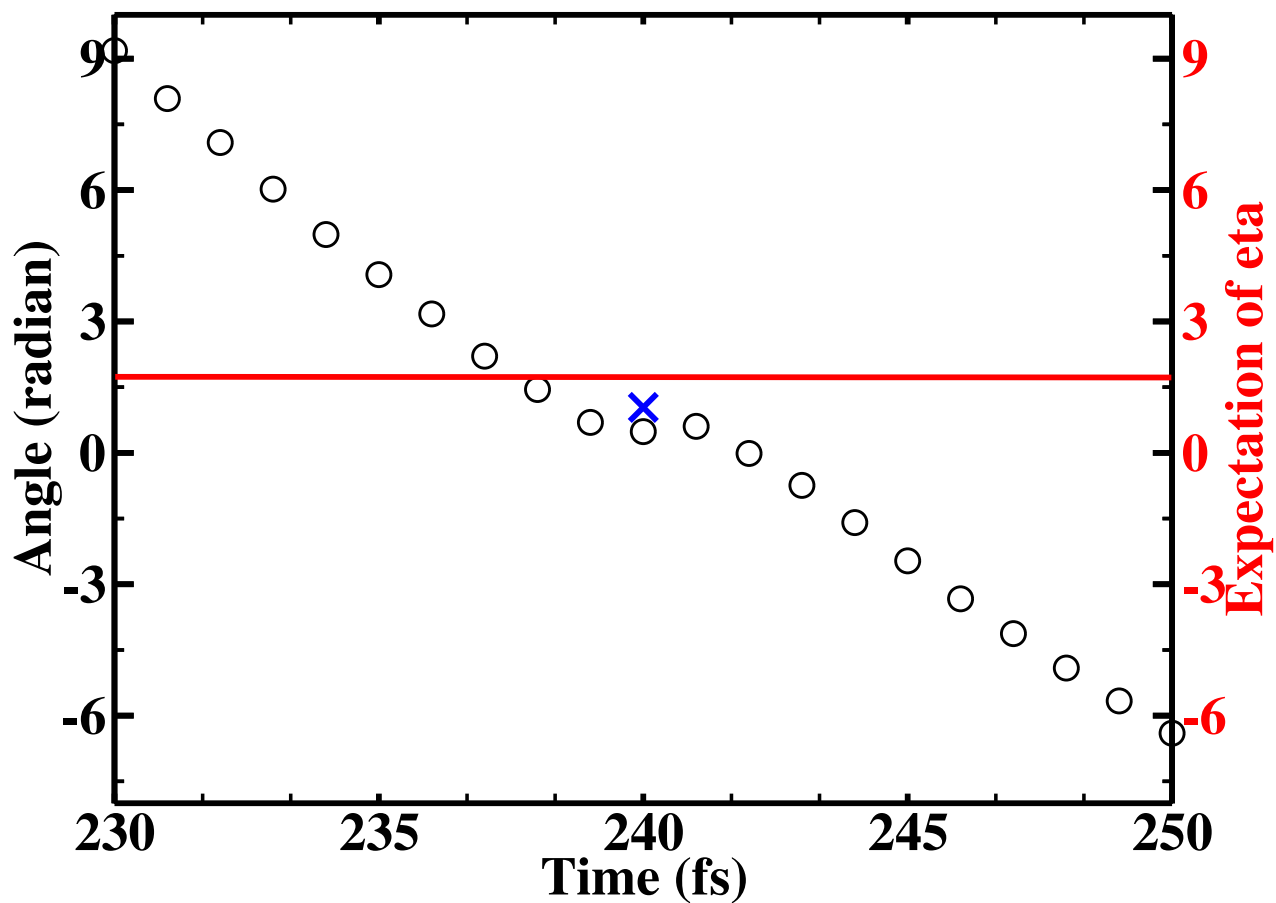


(d) Time-dependent phase of the 3D CHO model for H + H<sub>2</sub>

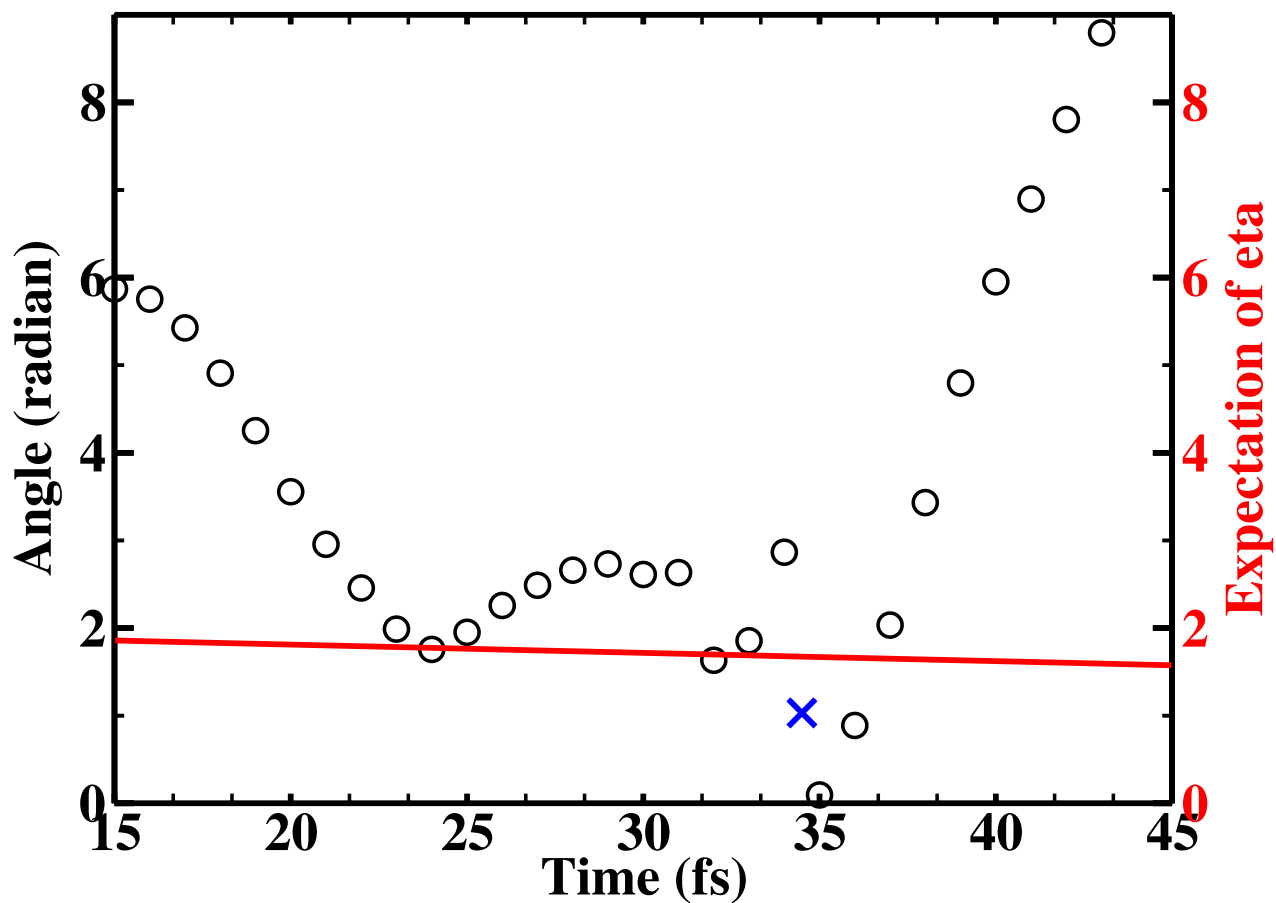
FIG. 4: Phase Expert, Meng



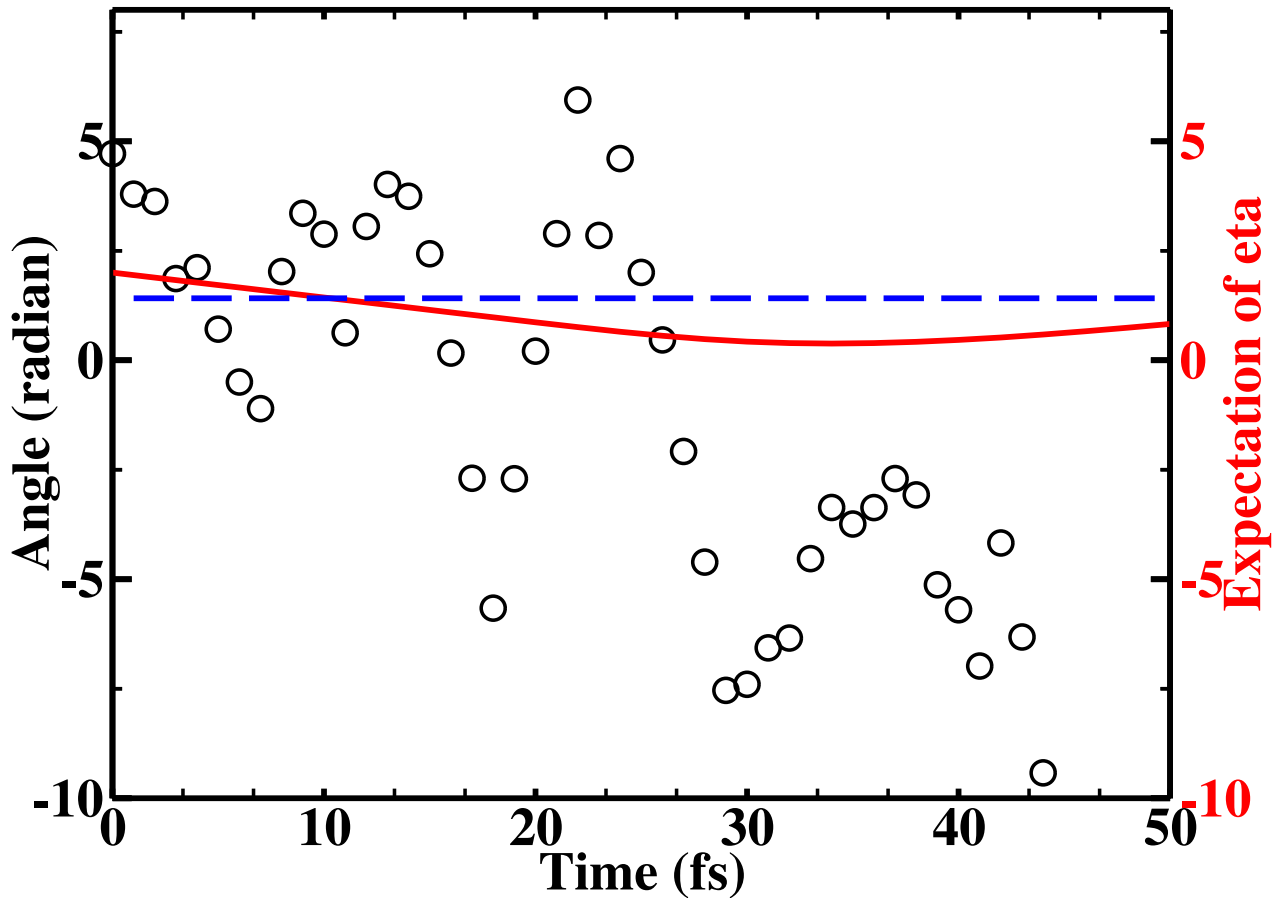
(a) Time-dependent phase of the 3D REX model for CO/Cu



(b) Time-dependent phase of the 3D REX model for CH<sub>4</sub>/Au



(c) Time-dependent phase of the 3D REX model for H<sub>2</sub>O



(d) Time-dependent phase of the 3D REX model for H + H<sub>2</sub>

FIG. 5: Phase Expert, Meng

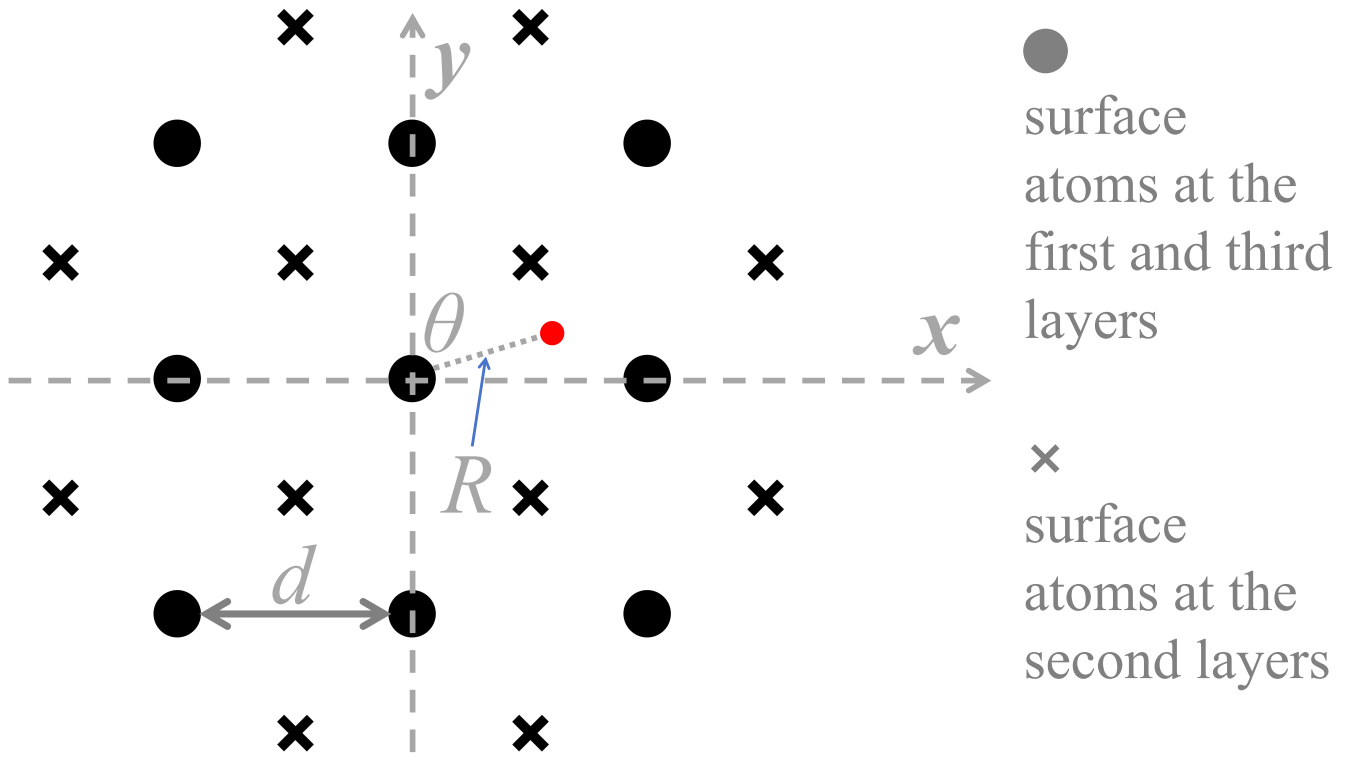
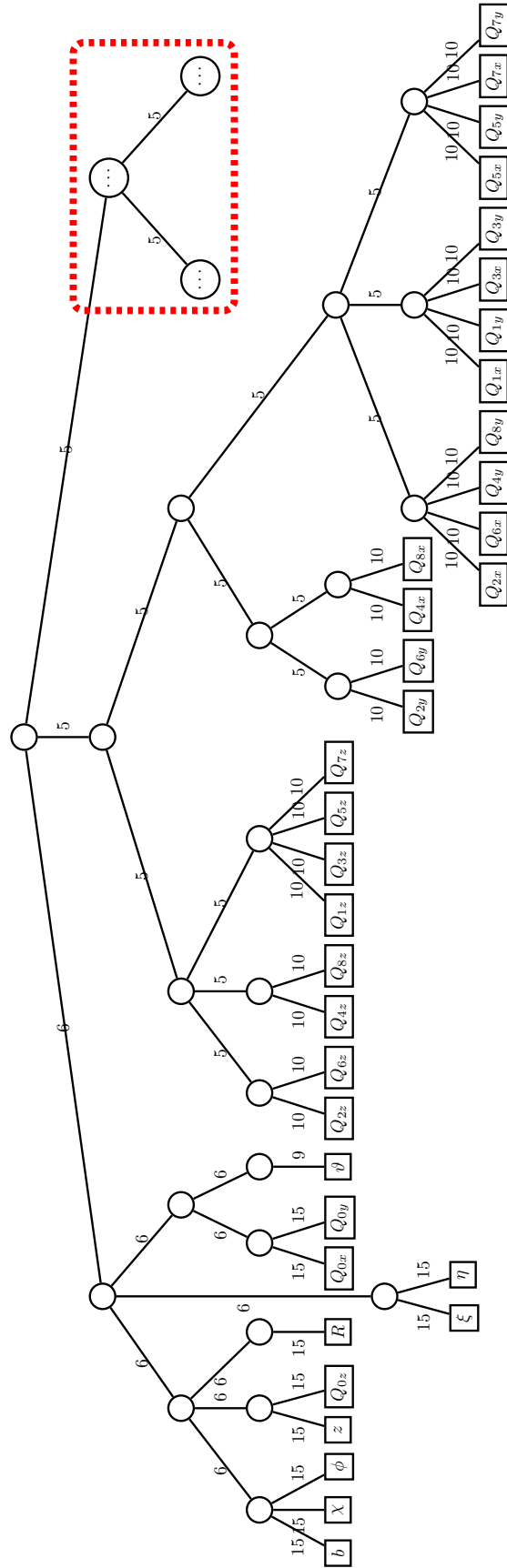
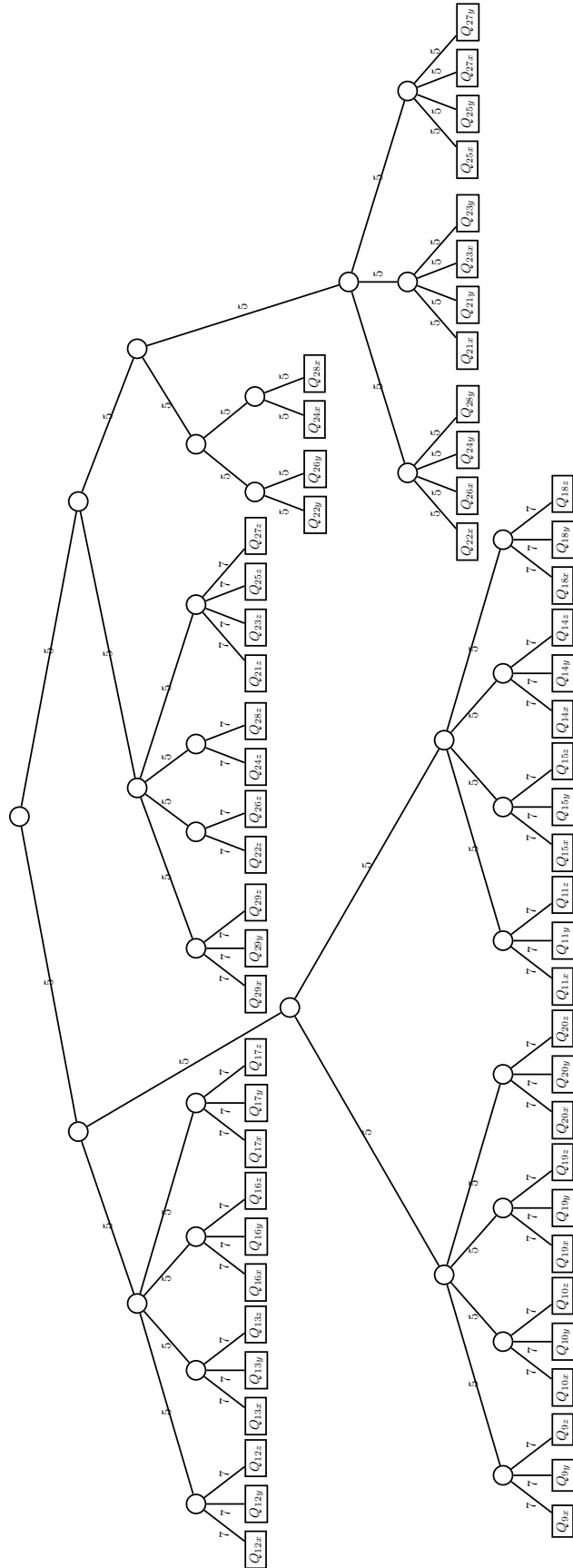


FIG. 6: Phase Expert, Meng



(a) ML-tree of the entire wave function



(b) ML-tree for the other part

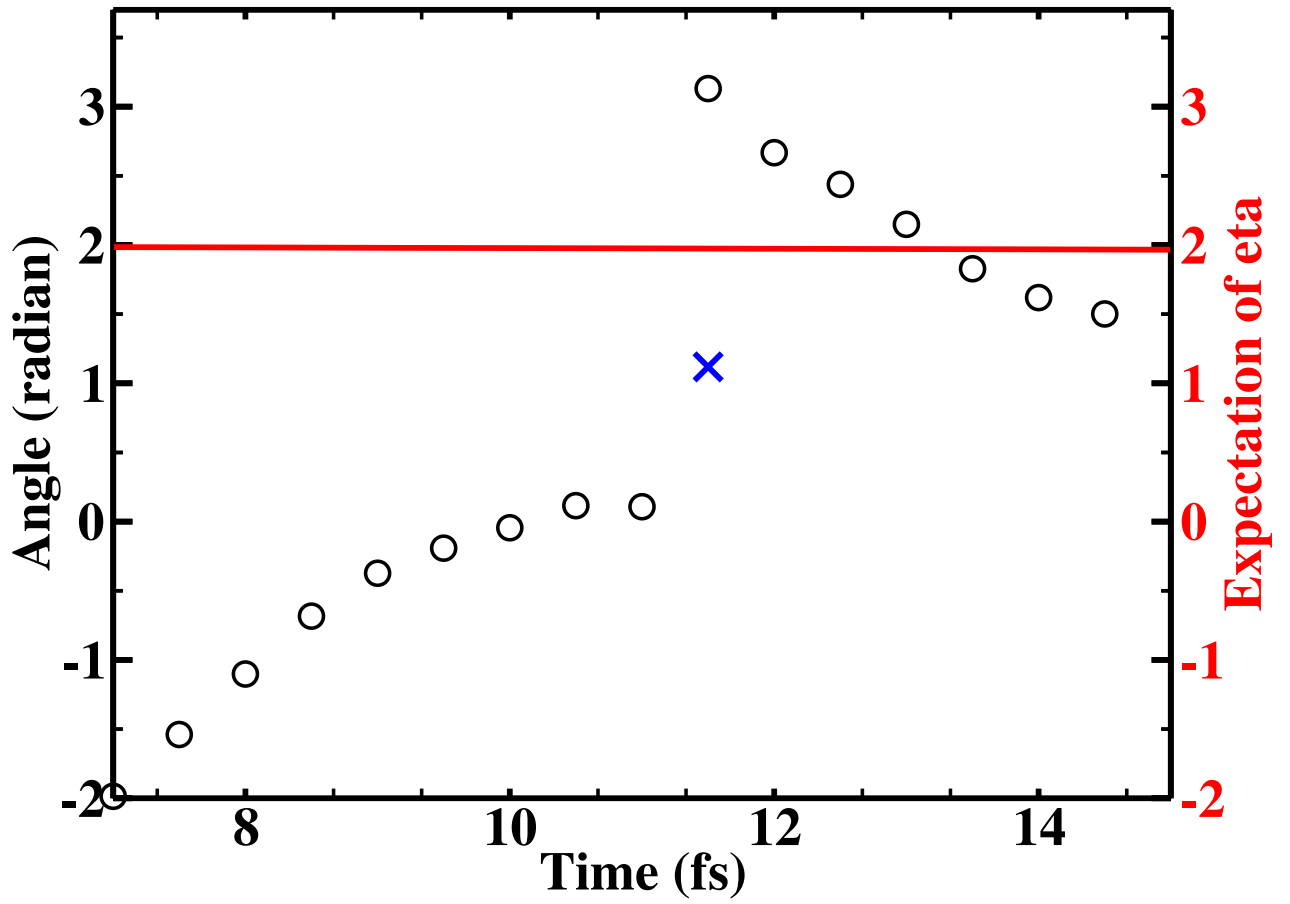


FIG. 8: Phase Expert, Meng

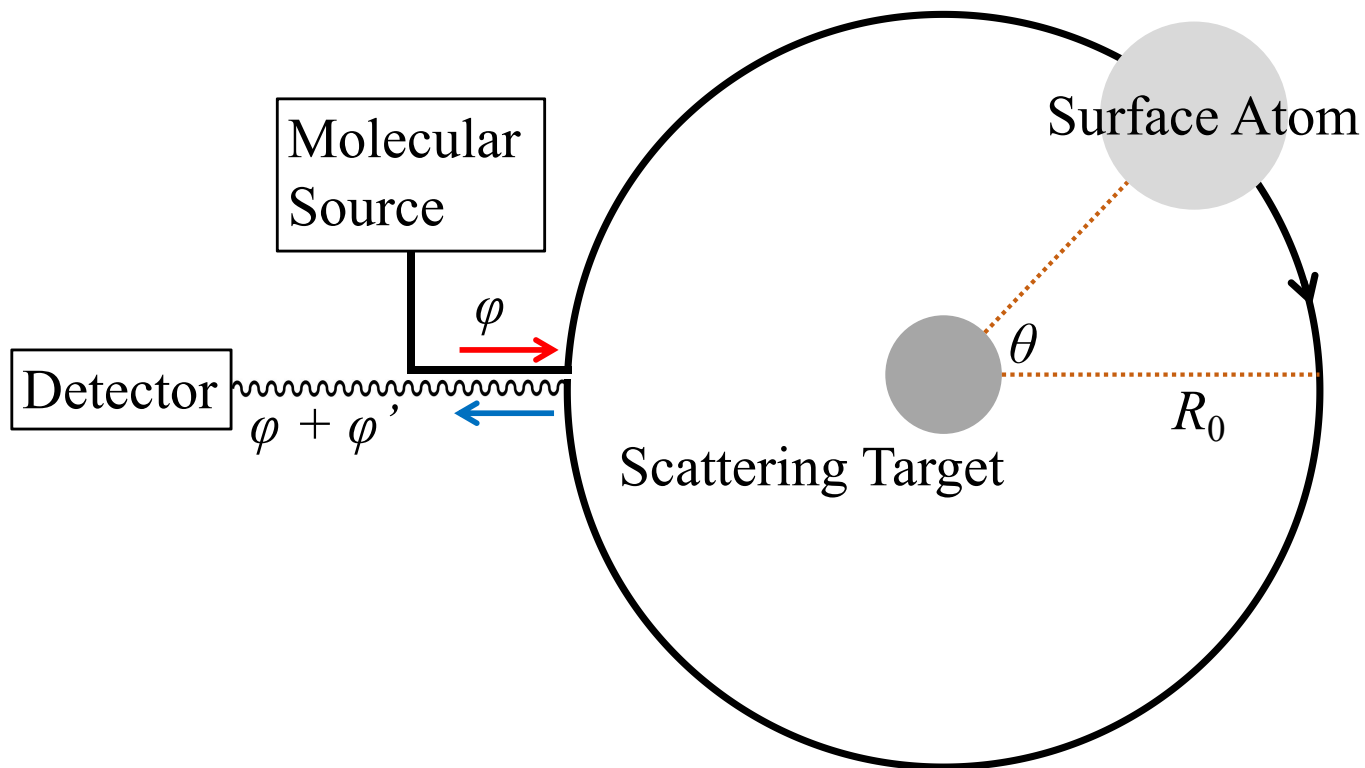


FIG. 9: Phase Expert, Meng

## REFERENCES

- <sup>1</sup>L. S. Cederbaum. Born-oppenheimer approximation and beyond. In *Conical Intersections* (Singapore, 2004), W. Domcke, D. R. Yarkony, and H. Köppel, Eds., World Scientific Co., pp. 3–40.
- <sup>2</sup>M. Baer. *Beyond Born-Oppenheimer: Electronic Nonadiabatic Coupling Terms and Conical Intersections*. Wiley, Hoboken, NJ, 2006.
- <sup>3</sup>L. S. Cederbaum. *J. Chem. Phys.* **138** (2013), 224110.
- <sup>4</sup>D. Xiao, M.-C. Chang, and Q. Niu. *Rev. Mod. Phys.* **82** (2010), 1959–2007.
- <sup>5</sup>M. V. Berry. *Proc. R. Soc. A* **392** (1984), 45.
- <sup>6</sup>D. Yuan, Y. Guan, W. Chen, H. Zhao, S. Yu, C. Luo, Y. Tan, T. Xie, X. Wang, Z. Sun, D. H. Zhang, and X. Yang. *Science* **362** (2018), 1289.
- <sup>7</sup>T. Yang and X. Yang. *Science* **368** (2020), 582–583.
- <sup>8</sup>Y. Xie, H. Zhao, Y. Wang, Y. Huang, T. Wang, X. Xu, C. Xiao, Z. Sun, D. H. Zhang, and X. Yang. *Science* **368** (2020), 767.
- <sup>9</sup>W. Chen, R. Wang, D. Yuan, H. Zhao, C. Luo, Y. Tan, S. Li, D. H. Zhang, X. Wang, Z. Sun, and X. Yang. *Science* **371** (2021), 936–940.
- <sup>10</sup>X. Wang and X. Yang. *Science* **374** (2021), 938–939.
- <sup>11</sup>H. Pan and K. Liu. *Nat. Chem.* **14** (2022), 545–549.
- <sup>12</sup>Y. Wang, J. Huang, W. Wang, T. Du, Y. Xie, Y. Ma, C. Xiao, Z. Zhang, D. H. Zhang, and X. Yang. *Science* **379** (2023), 191–195.
- <sup>13</sup>Z. Li, Y. lin Fu, Z. Luo, S. Yang, Y. Wu, H. Wu, G. Wu, W. Zhang, B. Fu, K. Yuan, D. Zhang, and X. Yang. *Science* **383** (2024), 746–750.
- <sup>14</sup>C. S. Reilly, D. J. Auerbach, L. Zhang, H. Guo, and R. D. Beck. *Science* **387** (2025), 962–967.
- <sup>15</sup>Q. Meng and H.-D. Meyer. *J. Chem. Phys.* **143** (2015), 164310.
- <sup>16</sup>Q. Meng, J. Chen, J. Ma, X. Zhang, and J. Chen. *Phys. Chem. Chem. Phys.* **24** (2022), 16415–16436.
- <sup>17</sup>J. C. Polanyi. *Angew. Chem. Int. Ed.* **26** (1987), 952–971.
- <sup>18</sup>J. C. Polanyi. *Science* **236** (1987), 680–690.
- <sup>19</sup>Q. Meng and H.-D. Meyer. *J. Chem. Phys.* **146** (2017), 184305.
- <sup>20</sup>A. I. Boothroyd, W. J. Keogh, P. G. Martin, and M. R. Peterson. *J. Chem. Phys.* **104** (1996), 7139.
- <sup>21</sup>Z. Bačić and J. C. Light. *Ann. Rev. Phys. Chem.* **40** (1989), 469.

- <sup>22</sup>S. Sukiasyan and H.-D. Meyer. *J. Phys. Chem. A* **105** (2001), 2604–2611.
- <sup>23</sup>H. Wang and M. Thoss. *J. Chem. Phys.* **119** (2003), 1289–1299.
- <sup>24</sup>U. Manthe. *J. Chem. Phys.* **128** (2008), 164116.
- <sup>25</sup>O. Vendrell and H.-D. Meyer. *J. Chem. Phys.* **134** (2011), 044135.
- <sup>26</sup>H. Wang. *J. Phys. Chem. A* **119** (2015), 7951.
- <sup>27</sup>G. A. Worth, M. H. Beck, A. Jäckle, O. Vendrell, and H.-D. Meyer. The MCTDH Package, Version 8.2, (2000). H.-D. Meyer, Version 8.3 (2002), Version 8.4 (2007). O. Vendrell and H.-D. Meyer Version 8.5 (2013). Version 8.5 contains the ML-MCTDH algorithm. Current versions: 8.4.18 and 8.5.11 (2019). See <http://mctdh.uni-hd.de/>.
- <sup>28</sup>A. Jäckle and H.-D. Meyer. *J. Chem. Phys.* **104** (1996), 7974.
- <sup>29</sup>A. Jäckle and H.-D. Meyer. *J. Chem. Phys.* **109** (1998), 3772.
- <sup>30</sup>Q. Song, Q. Zhang, and Q. Meng. *J. Chem. Phys.* **151** (2019), 114302.
- <sup>31</sup>H.-D. Meyer, U. Manthe, and L. S. Cederbaum. *Chem. Phys. Lett.* **165** (1990), 73–78.
- <sup>32</sup>M. H. Beck, A. Jäckle, G. A. Worth, and H.-D. Meyer. *Phys. Rep* **324** (2000), 1–105.
- <sup>33</sup>H.-D. Meyer, F. Gatti, and G. A. Worth, Eds. *Multidimensional Quantum Dynamics: MCTDH Theory and Applications*. Wiley-VCH, Weinheim, 2009.
- <sup>34</sup>H.-D. Meyer. *WIREs: Comput. Mol. Sci.* **2** (2012), 351–374.
- <sup>35</sup>H.-D. Meyer and H. Wang. *J. Chem. Phys.* **148** (2018), 124105.
- <sup>36</sup>H. Wang and H.-D. Meyer. *J. Chem. Phys.* **149** (2018), 044119.
- <sup>37</sup>Q. Meng, M. Schröder, and H.-D. Meyer. *J. Chem. Theory Comput.* **17** (2021), 2702–2713.
- <sup>38</sup>X.-G. Wang and E. L. Sibert III. *J. Chem. Phys.* **111** (1999), 4510.
- <sup>39</sup>S. Yoon, R. J. Holiday, I. Sibert, Edwin L., and F. F. Crim. *J. Chem. Phys.* **119** (2003), 9568–9575.
- <sup>40</sup>Q. Meng and H.-D. Meyer. *J. Chem. Phys.* **139** (2013), 164709.